

The X-ray footprint of the CircumNuclear Disk

Enmanuelle Mossoux¹[★] and Andreas Eckart^{2,3}

¹*Space sciences, Technologies and Astrophysics Research (STAR) Institute, Université de Liège, Allée du 6 Août, 19c, Bât B5c, 4000 Liège, Belgium*

²*Physikalisches Institut der Universität zu Köln, Zùlpicher Str. 77, D-50937 Köln, Germany*

³*Max-Planck-Institut für Radioastronomie, Auf dem Hügel 69, D-53121 Bonn, Germany*

Accepted XXX. Received YYY; in original form ZZZ

ABSTRACT

We studied the central regions of the Galactic Centre to determine if the CircumNuclear Disk (CND) acts as an absorber or a barrier for the central X-rays diffuse emission. After reprocessing 4.6 Ms of Chandra observations, we were able to detect, for the first time, a depression in the X-ray luminosity of the diffuse emission whose size and location correspond to those of the CND. We extracted the X-ray spectra for various regions inside the CND footprint as well as for the region where the footprint is observed and for a region located outside the footprint. We simultaneously fitted these spectra as an optically thin plasma whose absorption by the interstellar medium and by the local plasma were fitted independently using the MCMC method. The hydrogen column density of the ISM is $7.5 \times 10^{22} \text{ cm}^{-2}$. The X-ray diffuse emission inside the CND footprint is formed by a 2T plasma of 1 and 4 keV with slightly super-solar abundances except for the iron and carbon which are sub-solar. The plasma from the CND, in turn, is better described by a 1T model with abundances and local hydrogen column density which are very different to those of the innermost regions. The large iron abundance in this region confirms that the CND is dominated by the shock-heated ejecta of the Sgr A East supernova remnant. We deduced that the CND rather acts as a barrier for the Galactic Centre plasma and that the plasma located outside the CND may correspond to the collimated outflow possibly created by Sgr A* or the interaction between the wind of massive stars and the mini-spiral material.

Key words: Galaxy: centre – X-rays: individual: Sgr A*

1 INTRODUCTION

The Sgr A complex at the centre of the Milky Way (with a distance of about 8 kpc; Genzel et al. 2010; Falcke & Markoff 2013) is composed by several structures (Herrnstein & Ho 2005) observed in radio, near-infrared (NIR) and X-rays. Sgr A East is a supernovae remnant (SNR) whose the shell encloses a hot plasma radiating in X-rays via non-thermal emission (Ekers et al. 1983). In radio, the most luminous part of Sgr A East is a $10^4 M_{\odot}$ torus of neutral gas named the CircumNuclear Disk (CND) located at about 30 arcsec from the Galactic Centre supermassive black hole Sgr A* (Eckart & Genzel 1999). The CND is observed in radio/sub-millimetre (Sjouerman & Pihlström 2008; Martín et al. 2012) and far infrared (Lau et al. 2013). Sgr A West hosts Sgr A* whose the bolometric luminosity is 10^{-9} times smaller than the Eddington luminosity $L_{\text{Edd}} = 3 \times 10^{44} \text{ erg s}^{-1}$ (Yuan et al. 2003)

for a black hole mass of about $4 \times 10^6 M_{\odot}$ (Schödel et al. 2002; Ghez et al. 2008; Gillessen et al. 2009).

The X-ray diffuse emission at the Galactic Centre was first observed with Chandra on 1999 Sept. 21 (Baganoff et al. 2003). Its spectrum within 10 arcsec ($\sim 0.4 \text{ pc}$) from Sgr A* obtained during this Chandra observation was fitted with a thermal Bremsstrahlung characterized by a temperature of $\kappa T = 1.6 \text{ keV}$ and a hydrogen column density of $N_{\text{H}} = 10.1 \times 10^{22} \text{ cm}^{-2}$. They also fitted its spectrum using the optically thin plasma model of Raymond & Smith (1977) with twice the solar abundances leading to $\kappa T = 1.3 \text{ keV}$ and $N_{\text{H}} = 12.8 \times 10^{22} \text{ cm}^{-2}$.

The innermost X-ray diffuse emission is likely produced by the interaction of the winds of the massive stars located in the central parsec star cluster (Krabbe et al. 1991; Genzel et al. 2003). These stars are probably the first source of fresh matter feeding Sgr A*. Quataert (2004) determined the density and temperature distributions of the plasma within the central 30 arcsec ($\sim 1 \text{ pc}$) by modelling massive stars with a wind velocity of 1000 km s^{-1} and a mass loss

[★] E-mail: emossoux@ulg.ac.be

rate of $10^{-3} M_{\odot} \text{yr}^{-1}$ as the source of mass and energy for the dynamics of the hot gas. He found that the temperature and the density follow three different distributions according to the radial distance: $\kappa T \propto r^{-0.5}$ and $\rho \propto r^{-0.7}$ below 2arcsec; $\kappa T \propto r^{-0.1}$ and $\rho \propto r^{-1.3}$ between 2 and 10arcsec; and $\kappa T \propto r^{-1.4}$ and $\rho \propto r^{-2.6}$ between 10 and 30arcsec.

Sakano et al. (2004) used the XMM-Newton observation of 2001 Sept. 4 to study the spectra extracted from regions of 28, 60 and 100arcsec-radius centred on the maximum emission region of the 6.7keV emission line. They determined that the diffuse emission is produced by a two-temperature plasma with 2.5 times the solar abundances and temperatures of about 1 and 4keV.

The central gas within 1arcsec around Sgr A* is well described by the hot accretion flow models (for a review see Yuan & Narayan 2014 and references therein) such as radiatively inefficient accretion flow (RIAF; Yuan et al. 2003). Wang et al. (2013) showed that the X-ray spectrum of the 1.5arcsec region around Sgr A* observed during the 2012 Chandra X-ray Visionary Project (XVP) is well fitted by the RIAF model whose the differential emission measure varies as $T^{-1.9}$. They determined a hydrogen column density of about $14 \times 10^{22} \text{cm}^{-2}$.

In the present work, we used the overall Chandra observations of the Galactic Centre from Sept. 1999 to Oct. 2012 (for a total exposure of about 4.6Ms) to constrain the characteristics of the X-ray diffuse emission from 1.5 to 70arcsec. We did not use the data obtained between 2013 and 2015 because of the presence of several transient sources at the Galactic Centre: SGR J1745-29 (e.g. Dwelly & Ponti 2013; Kennea et al. 2013; Gehrels et al. 2013), SWIFT J174540.7-290015 (Reynolds et al. 2016) and SWIFT J174540.2-290037 (Degenaar et al. 2016). Thanks to these 4.6Ms of observations whose data reduction is presented in Sect. 2, we detected a depression in the X-ray diffuse emission whose the location and size correspond to those of the CND (Sect. 3). We then compared the characteristics of the X-ray emission within the CND footprint with those of the innermost and outermost regions (Sect. 4). We discussed the physical characteristics and determined the role of the CND in Sect. 5 and summarized our results in Sect. 6.

2 OBSERVATIONS AND DATA REDUCTION

We used the 1999–2012 Chandra data available from the Chandra Search and Retrieval interface (ChaSeR)¹. We limited our study to the observations where Sgr A* was observed with an off-axis angle lower than 2arcmin. We thus studied 84 observations obtained with the ACIS-I or ACIS-S/HETG cameras (Garmire et al. 2003) leading to a total exposure of 4.6Ms.

We reduced these data using the Chandra Interactive Analysis of Observations (CIAO) package (version 4.7) and the Calibration Database (CALDB; version 4.6.9) as the following: we first reprocessed the level 1 data using the CIAO script `chandra_repro` to filter the event patterns, afterglow events and bad-pixel events. We also filtered out the time intervals contaminated by soft protons flares.

For the observations made with the High Energy Transmission Grating (HETG), the diffraction order is determined with the CIAO task `tg_resolve_events`. We only selected the zero-order events.

3 THE X-RAY DIFFUSE EMISSION WITHIN 200 ARCSEC \times 200 ARCSEC

Since our study is about the X-ray diffuse emission in the central parsecs of the Milky Way, we only selected the events recorded in a 200arcsec \times 200arcsec region ($\sim 7.8 \times 7.8 \text{pc}$) centred on the Sgr A* radio position (RA(J2000) = $17^{\text{h}}45^{\text{m}}40^{\text{s}}.036 \pm 1.42 \text{mas}$, Dec(J2000) = $-29^{\circ}00'28''.17 \pm 2.65 \text{mas}$; Petrov et al. 2011). We created an image of this region by merging the filtered event lists of the 84 observations. We first reprojected the events on the Sgr A* position using the `reproject_obs` CIAO task. We then created exposure-corrected² images for the ACIS-I or ACIS-S/HETG cameras from the reprojected event lists using the `flux_obs` CIAO task. The two images were then summed and corrected from the exposure time ratio. The resulting image is shown in the right panel of Fig. 1.

One can observe that the diffuse emission is not symmetrically distributed and extends towards the North-East of Sgr A*. Moreover, a depression in the X-ray luminosity at about 30arcsec from Sgr A* is noticeable especially towards the North-East and the West directions. Such a depression was already discernible in the Galactic Centre X-ray images published in previous studies (e.g., Wang et al. 2006; Li et al. 2013; Lau et al. 2015) but none of these authors studied the nature of this feature.

To determine the position and the shape of this depression, we assumed a symmetrical distribution of the X-ray diffuse emission centred on the Sgr A* position. In this particular approach we used a Gaussian distribution and estimated the amplitude of the Gaussian from the peak count-rate of the X-ray image in a region of 10arcsec-radius centred on Sgr A* where the point sources (Sgr A*, the complex of massive stars IRS13 and the pulsar wind nebulae G359.950.04) were removed. The Gaussian amplitude is about 30 times less than the peak average flux at the position of Sgr A* and about 3 times less than the emission just 3–5arcsec Southwest of it. By visual inspection we approximated the distribution of diffuse emission by a Gaussian of 90arcsec \times 60arcsec FWHM at a position angle of -30° , i.e. along the Galactic plane. The resulting image is little dependent on the assumptions as long as the component includes most of the diffuse emission along the Galactic plane. In Fig. 1, we show the Gaussian component model of the X-ray diffuse emission on the left in comparison to the Chandra X-ray image on the right. In Fig. B1 in the Appendix B we show the results of several different attempts to extract the structure.

In order to investigate the distribution of the absorbing material, we subtracted the X-ray image from the Gaussian model of the diffuse emission. Setting all negative components (i.e., emission) to zero and convolving with a 5arcsec

¹ <http://cda.harvard.edu/chaser>

² This includes the correction of the quantum efficiency, effective area and exposure time.

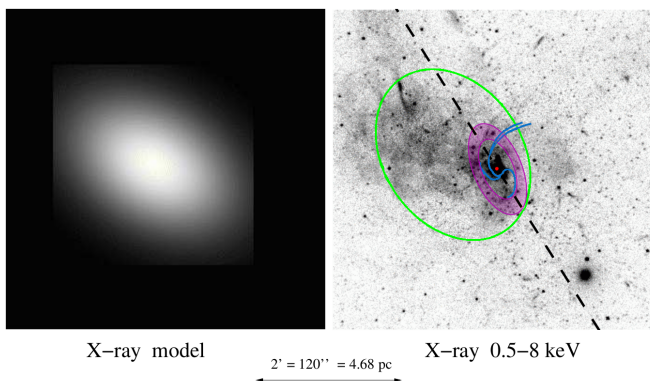


Figure 1. *Left panel:* The Gaussian model for the X-ray diffuse emission. *Right panel:* The Chandra image of the X-ray diffuse emission and point-like sources at the Galactic Centre observed between 0.5 and 8 keV from 1999 to 2012. The pixel size is 0.5 arcsec corresponding to the Chandra angular resolution. The image intensity (count rate) is in inverted logarithmic scale (the brightest regions have the darkest colour). We also over-plotted the schematic diagram of the main features of the Sgr A complex adapted from Baganoff et al. (2003). The dashed line is the Galactic plane direction, the blue lines are Sgr A West, the magenta torus is the CND, the green ellipse is Sgr A East and the red point is Sgr A*. (See online for colour version.)

FWHM Gaussian, we obtained a positive image of the sought for absorbing components (see right panel of Fig. 2).

The upper panels of Fig. 2 show a comparison between the X-ray depression and the integrated CN(2-1) (226.875 GHz) and the $N_2H^+(1-0)$ (93.173 GHz) line emissions (Martín et al. 2012; Moser et al. 2017). The CN(2-1) contour map highlights the presence of a Southwest and Northeast lobe (in the nomenclature of Martín et al. 2012) whose position is indicated by the arrows in the X-ray image. In these panels, we highlighted by two thick continuous lines (black and yellow) the circumference of the deepest X-ray depression regions that we derived. These regions are in good agreement with the molecular part of the CND. The lower panels of Fig. 2 compare the image of the JHK (1.19 μm , 1.71 μm , and 2.25 μm) continuum extinction map (Nishiyama & Schödel 2013) of the foreground dust components taken with the ISAAC at the ESO VLT (Moorwood et al. 1998) with the X-ray depression. In the bottom left panel, we highlighted prominent dust extinction patches (labelled α to ϵ) as well as a dashed line that includes the less extinguished part of the central stellar cluster. One can observe a very good agreement between the depression and the dashed line as well as between the dust patches and the less luminous parts of the X-ray depression.

Two interpretations may explain the observed depression: the first one is that the plasma creating the diffuse emission is physically arrested by the CND because of a difference of density and pressure between the inner plasma and those of the CND. The second one is that the CND is located between the observer and the source of the diffuse

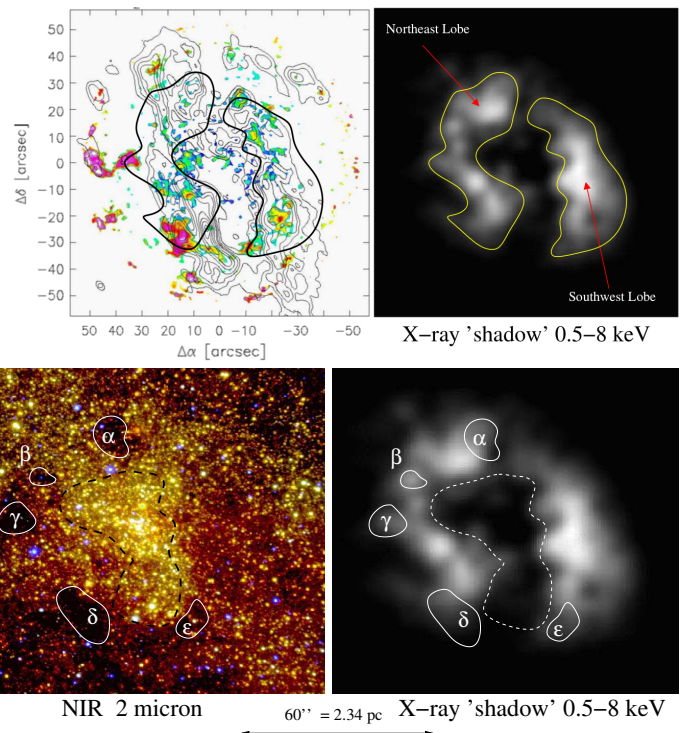


Figure 2. Comparison of the X-ray footprint of the CND with the infrared and radio images of the CND. *Top left panel:* The radio image of the CND taken from Fig. 4 of Moser et al. (2017). The contour map is the CN(2-1) emission while the colour map is the $N_2H^+(1-0)$ emission. *Bottom left panel:* The JHK (1.19 μm , 1.71 μm , and 2.25 μm) continuum extinction map (Nishiyama & Schödel 2013) of the foreground dust components taken with the ISAAC at the ESO VLT (Moorwood et al. 1998). A 103 arcsec \times 103 arcsec field is shown. *Right panels:* The image of the CND footprint in X-rays convolved with a 5 arcsec-FWHM Gaussian, scaled to the image sizes shown on the left. The brighter the region, the larger the absorption. (See online for colour version.)

emission diffuse emission and absorbs the X-ray photons. Physically, it may be expected that the two scenarios occurs jointly with the CND acting as a barrier for a inner plasma and as an absorber for a background plasma. However, considering jointly the two scenarios implies the determination of the exact 3D shape of the source of the Galactic Centre emission which is well beyond the scope of this study since the resolution and the accuracy of the spectral parameters determined with the X-ray data are not enough to answer this question. In the present paper, we will thus rather consider the two scenarios independently to determine what is the dominant interpretation. The two interpretations could be distinguished by analysing the spectra of the diffuse emission in the central region and those extracted from an annulus region corresponding to the CND footprint location.

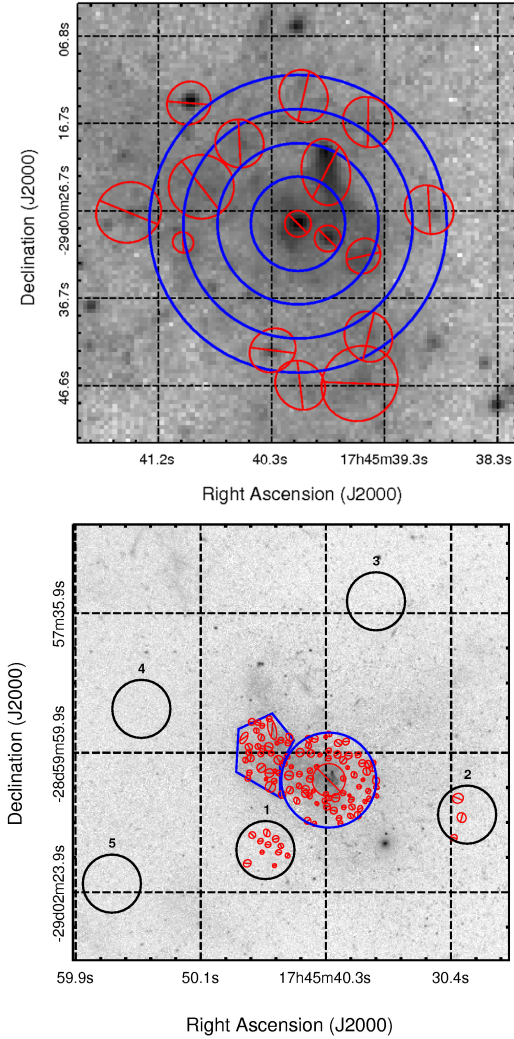


Figure 3. The spectrum extraction regions. *Top panel:* X-ray image of the central $50\text{arcsec} \times 50\text{arcsec}$. The concentric annuli for the study of the X-ray diffuse emission in the innermost regions are shown in blue. The red regions are the point source regions computed with the CIAO task `wavdetect` and excluded from the spectrum extraction regions. *Bottom panel:* X-ray image of the central $450\text{arcsec} \times 450\text{arcsec}$. The blue circle is the outer radius of the CNDF footprint. The inner radius of this region is the largest red circle centred on the Sgr A* position. The blue polygon is the extraction region corresponding to the diffuse emission “outside” the CNDF. The black circles are the different background regions. (See online for colour version.)

4 THE SPECTRA OF THE X-RAY DIFFUSE EMISSION

4.1 Spectrum extraction

We defined four source+background (src+bkg) regions inside the CNDF footprint to study the variation of the physical characteristics of the plasma with the radial distance. To do so, we created four concentric annuli from 1.5 to 17 arcsec with a difference between the outer and the inner radius of 3.9 arcsec. These regions are represented in blue in the top panel of Fig. 3. We then defined the CNDF region as an annulus centred on Sgr A* with an inner radius of 17 arcsec and

a outer radius of 49 arcsec. The inner and outer radii were defined to include 90% of the image intensity in the right panels of Fig. 2 and were not corrected from the inclination angle of the CNDF. The spectrum of the plasma “outside” the CNDF was extracted from a polygonal region at the North-East of Sgr A* where the emission is the highest to increase the signal-to-noise ratio. The centre of this region is located at about 70 arcsec from Sgr A*. These two last regions are shown in blue in the bottom panel of Fig. 3.

We then searched for the point sources in the exposure-corrected image of the Galactic Centre using the `wavdetect` CIAO script (Freeman et al. 2002) with a “Mexican hat” wavelet whose the scale increases from 1 to 16 by a factor $\sqrt{2}$ and with a sensitivity threshold of 10^{-7} as it was done by Munro et al. (2003). We detected 256 X-ray sources which were removed from the spectrum extraction regions defined above.

The completeness limit of this search method for the Galactic Centre is about $2 \times 10^{31} \text{ergs}^{-1}$ (Munro et al. 2003). The contribution of fainter stars such as young stellar objects (YSOs) or cataclysmic variables (CVs) in the X-ray diffuse emission is not easily computable. However, Munro et al. (2004) determined that the number of undetected YSOs and CVs is about ten times smaller than the number of sources required to create the hot emission at the Galactic Centre. They also determined that the softer diffuse emission is predominantly heated by a supernovae remnant. We clearly observe in the right panel of Fig. 1 that the diffuse emission is not symmetrically distributed around Sgr A*. If this diffuse emission is predominantly produced by undetected point-like sources, it is difficult to explain why these sources are not symmetrically distributed around Sgr A*. We thus considered that the contribution of undetected sources in the diffuse emission spectra is negligible.

The instrumental background contribution was estimated by extracting events from a large background (bkg) region located on the same CCD than the src+bkg regions where the X-ray diffuse emission is minimum. To test the effect of the background subtraction on the spectral fitting, we selected five 30 arcsec-circular apertures at different locations on the CCD (black circles labelled “1” to “5” in the bottom panel of Fig. 3).

The src+bkg and bkg spectra as well as the corresponding Ancillary Response Files (ARF) and Redistribution Matrix Files (RMF) were computed together using the CIAO `specextract` script for each extraction region and the overall 84 observations. Because of the large surface of the extraction regions, we weighted the ARF over the region areas thanks to the “weight=yes” option. For each region, we combined the spectra observed with ACIS-I (46 spectra) and ACIS-S/HETG (38 spectra) separately thanks to the “combine=yes” option. The spectrum merging is allowed in our study since the merged data have the same clocking mode, the same Science Instrument Module (SIM) position, a close spacecraft orientation and the same detector configuration. Moreover, the data have been reprocessed with the same Calibration Database and we merged the spectra extracted from the same region. We thus have two spectra for each of the six regions. Finally, we grouped the spectra from the

minimum energy of 1 keV with a minimum signal-to-noise ratio of 10³.

In each spectrum, we observed several emission lines already detected by Wang et al. (2013) and Munro et al. (2004): the S XV K α and K β lines at 2.4 and 2.8 keV, the Ar XVII and Ar XVIII K α lines at 3.1 and 3.3 keV, the Ca XIX K α line at 3.9 keV, the Fe XXV K α and K β at 6.7 and 7.8 keV and the Fe XXVI K α line at 6.97 keV. The S XV K β was not detected by Wang et al. (2013) because of the small flux of this emission line and the lower number of observations they used (they only used the data from the 2012 Chandra XVP campaign). Munro et al. (2004) did not detect the Fe XXV K β line since they only studied the spectrum up to 8 keV.

4.2 Spectrum fitting

We first modelled the spectra as a one-temperature, optically thin plasma in collisional ionization equilibrium with the Astrophysical Plasma Emission Code VAPEC (Smith et al. 2001) and AtomDB v2.0.2. The plasma modelling of the emission is supported by its asymmetrical distribution around Sgr A* which likely exclude a pure CVs heating. We also took into account the absorption of X-ray photons because of the photo-ionization (modelled with TBnew⁴) and the dust scattering (modelled with dustscat; Predehl & Schmitt 1995) along the line-of-sight. TBnew uses the interstellar medium (ISM) abundances updated by Wilms et al. (2000) and the updated cross sections of Verner et al. (1996). We left free the relative abundances of the atoms creating the main emission lines. The abundance of the trace elements was set to solar. The pileup was also taken into account using the Davis (2001)'s model available in XSPEC (version 12.9.0d) with the photon migration parameter $\alpha = 1$ (Nowak et al. 2012; Neilsen et al. 2013) and a PSF fraction of 95%. The model used to fit the spectra in XSPEC is thus `pileup*dustscat*TBnew*VAPEC`. The model parameters are the hydrogen column density N_{H} with $N_{\text{H,dustscat}} = N_{\text{H,TBnew}}/1.5$, the VAPEC normalization N , the plasma temperature kT and the abundances of the atoms producing the main emission lines: n_{S} , n_{Ar} , n_{Ca} , n_{Fe} . The abundances of He, N, O, Ne, Mg, Al, Si and Ni were assumed to be equal to those of C as it was done by Wang et al. (2013). We thus have eight free model parameters. The model parameters for the ACIS-S and ACIS-I spectra extracted from the same extraction region are tied to the same value.

We simultaneously fitted the twelve src+bkg spectra, considering each of the five bkg spectra, using the Markov Chain Monte Carlo (MCMC) method which iteratively produces a set of model parameters by using a number of “walkers” evolving independently from each others in the parameter space. The model parameters converge towards their marginal distribution to describe the observed spectra. We used the Jeremy Sanders’ XSPEC_emcee⁵ program

with the Goodman & Weare (2010)'s affine invariant ensemble sampler that allows the MCMC analysis with XSPEC using emcee⁶, an extensible, pure-Python implementation of Goodman & Weare (2010)'s MCMC ensemble-sampler. This method reduces the auto-correlation time of the model parameters. Following Foreman-Mackey et al. (2013), the number of walkers must be about 10 times the number of model parameters. The autocorrelation time τ_{f} which describe the number of steps needed to construct independent samples is computed thanks to the acor package (v1.1.1) available in Python⁷. The “burn-in” period rejected for the results analysis must be $20\tau_{\text{f}}$ and the length of the Markov chain must be 30 times the “burn-in” period to converge towards the target density (Foreman-Mackey et al. 2013). Following Gelman et al. (1996) and Foreman-Mackey et al. (2013), the acceptance fraction a_{f} , i.e., the number of steps which are accepted since their likelihood function is lower than those of the previous step, must range between 0.2 and 0.5. This number is an *a posteriori* proof of the convergence of the model parameters.

However, we could not reproduce together the flux of the low energy emission lines (such as S and Ar) and the flux of the Fe emission lines with this model. We thus fitted the spectra with a two-temperature plasma as proposed by Sakano et al. (2004) and Markoff (2010) using two VAPEC models with the same relative abundances but with different temperatures. Moreover, we improved our fitting model by separating the absorption by the ISM described by the hydrogen column density $N_{\text{H,ISM}}$ and the self-absorption by the gas at the Galactic Centre described by the local hydrogen column density $N_{\text{H,local}}$. Indeed, the hydrogen column density due to the ISM absorption must be the same for the overall spectra whereas the local absorption may vary because of the change of density and relative abundances of the plasma in different regions. This local absorption was modelled by vphabs which computes the photo-electric absorption. We tied the relative abundances of vphabs to those of the VAPEC model. We also tied the hydrogen column density of the ISM to the same value for the twelve src+bkg spectra.

We thus simultaneously fitted the twelve src+bkg spectra with the following model: `pileup*dustscat*TBnew*vphabs*(VAPEC+VAPEC)`. To reduce the number of spectral parameters, we also assumed that the abundances are constant below 17 arcsec since we are only interested by the comparison between the inner plasma and the CND plasma. We thus tied the abundances for the eight innermost src+bkg spectra to the same value. This model has 46 free model parameters for the twelve src+bkg spectra.

We performed the MCMC fitting five times in order to study the variation of the best fitting parameters with the position of the background extraction region. The best-fitting parameters are slightly dependent on the position of the bkg extraction region but their values are consistent within each other considering the error bars. We thus presented the results of the fit leading to the lowest reduced χ^2 .

³ The spectral grouping was obtained with ISIS which defined the signal-to-noise ratio as $(C_{\text{src}} - C_{\text{bkg}} \times \text{ratio}) / (C_{\text{src}} + C_{\text{bkg}} \times \text{ratio}^2)^{0.5}$ with *ratio* the exposure ratio multiplied by the region size ratio between the src+bkg and bkg spectrum and C_{src} and C_{bkg} the number of counts in the src+bkg and bkg spectrum, respectively.

⁴ <http://pulsar.sternwarte.uni-erlangen.de/wilms/research/tbabs/index.html>

⁵ <https://github.com/jeremysanders/xspec-emcee>

⁶ <http://dan.iel.fm/emcee/current/user/line/>

⁷ <https://pypi.python.org/pypi/acor/1.1.1>

The best fit is obtained using the bkg spectra extracted from the region 2. We observed that the best-fitting parameters of the CND region seems to reproduce one-temperature plasma. A F-test comparing the fits with a 2T and 1T model for the CND confirms that the data are better reproduced using only one temperature for the CND region. The auto-correlation time of the 44 model parameters is $\tau_f = 10.44$. The MCMC thus has 440 walkers walking simultaneously during 6027 steps after a “burn-in” period of 209 steps. The mean acceptance fraction after the “burn-in” period is $a_f = 0.17$ which corresponds to the range recommended by Gelman et al. (1996) and Foreman-Mackey et al. (2013).

The results of the MCMC fitting are represented in a triangle plot diagrams (created with the Python package `corner` v1.0.0) in Appendix A. These plots represent the values taken by all walkers at each step after the “burn-in” period. The marginal distributions of each spectral parameter are the diagonal plots. The best-fitting parameters are defined by the median of the marginal distributions. The joint distributions between each couple of parameters are shown in the other plots with the confidence levels at 68, 90 and 99%. The best-fitting parameters associated to each region and their 90% confidence level are given in Table 1. To compare the results, the normalization parameters of the two VAPEC models (N_1 and N_2) were normalized by the area of the extraction regions. The resulting spectra are shown in Fig. A11 in Appendix A.

We verified *a posteriori* that the 2T plasma model is better than a 1T model by performing a F-test. For the 1T model, the total χ^2 (i.e., for the twelve spectra) is 8984/1908 while for the 2T, the χ^2 is 3354/1898. The F-test probability is thus very low leading to the confirmation that the 2T temperature model better represents our set of spectra.

For the completeness of this study, we also tested a 2T plasma model where the foreground sources and soft diffuse emission were explicitly taken into account in the spectral fitting of the Galactic Centre diffuse emission. To do so, we first extracted the spectra of the 256 X-ray sources detected with `wavdetect` in Sect. 4.1. We fitted each spectrum using an absorbed powerlaw with `pileup*dustscat*TBnew*pegpwlw`. The unabsorbed flux in 2–10keV of these sources ranges from 2.2×10^{-14} to $3 \times 10^{-12} \text{ erg s}^{-1} \text{ cm}^{-2}$. The mean powerlaw index is about 1.7 with a minimum of 0.02 and a maximum of 4.3. The distribution of hydrogen column density is symmetric around a mean value of $9.95 \times 10^{22} \text{ cm}^{-2}$. The comparison of this distribution with the best-fitting value of $7.5 \times 10^{22} \text{ cm}^{-2}$ determined for the Galactic Centre diffuse emission (see Sect. 5.1) allows us to affirm that about 30% of the sources lies in the foreground of the Galactic Centre diffuse emission. The contribution of these foreground sources was thus modelled using an additional `pileup*dustscat*TBnew*pegpwlw` term to the 2T plasma model described above. We fixed the spectral index to 1.7 and the hydrogen column density to $5.2 \times 10^{22} \text{ cm}^{-2}$ which is the median value for the hydrogen column density distribution from the minimum value to $7.5 \times 10^{22} \text{ cm}^{-2}$. We left free the total flux of the sources for each of the six src+bkg regions. We also add a `pileup*dustscat*TBnew*cflux(pegpwlw + apec + vaped)` term to represent the foreground diffuse emission. This is the model used by Masui et al. (2009) to describe the soft diffuse emission out of the Galactic plane. Follow-

ing these authors, we fixed the hydrogen column density to $1.7 \times 10^{22} \text{ cm}^{-2}$, the spectral index to 1.5, the flux of the powerlaw between 0.5 and 10keV to $11.1 \times 10^{-12} \text{ erg s}^{-1} \text{ cm}^{-2}$, the APEC temperature to 0.105keV, the APEC normalisation to 14.1 cm^{-5} , the VAPEC temperature to 0.766keV, the oxygen abundance to 3.1 and the VAPEC normalisation to 3.75 cm^{-5} . We left free the flux between 0.5 and 10keV of the `cflux` component. We thus added twelve spectral parameters to our model. Unfortunately, the spectral fitting leads to large error bars on the spectral parameters because of the difficulty to disentangle between the Galactic Centre and foreground emission. However, it seems that the temperatures and hydrogen column densities derived for the Galactic Centre using this complex model are lower than without taking the foreground emission into account. But, due to the large error bars, we can not effectively conclude on the effects of the foreground emission on the spectral parameters from the Galactic Centre. The conclusions are the same considering a 1T model for the Galactic Centre plus the foreground emission.

What we can conclude is that the flux between 0.5 and 10keV for the foreground emission is about $6 \times 10^{-14} \text{ erg s}^{-1} \text{ cm}^{-2}$ which is about 7 times smaller than the flux computed for the Galactic Centre emission. We could thus conclude that the error on the normalization of the model for the Galactic Centre emission due to the failure of taking into account for the foreground emission is only 13%. This is in agreement with the fact that the shadow of the CND can readily be seen against the overall X-ray emission from that region.

In the following section, we will thus discuss the best-fitting parameters obtained with the model `pileup*dustscat*TBnew*vphabs*(VAPEC+VAPEC)`.

5 DISCUSSION

In this section, we will compare the characteristics of the plasma from the innermost and outermost regions to those from the CND region. The best-fitted parameters are not used here to deduce any physical mechanism occurring at the Galactic Centre and they are rather used to compare the general behaviour of the plasma between these regions. The evolution of the physical parameters with radial distance is shown in Fig. 4.

5.1 Hydrogen column density

The best-fitting hydrogen (neutral and ionized) column density of the ISM is $N_{\text{H,ISM}} = 7.5^{+0.2}_{-0.4} \times 10^{22} \text{ cm}^{-2}$ which is consistent with the lower limit of $6 \times 10^{22} \text{ cm}^{-2}$ determined by Munro et al. (2004). This value is close to the neutral hydrogen column density directly measured by Kalberla et al. (2005) using the 21-cm line. These authors determined that $N_{\text{HI}} = 12.2 \times 10^{22} \text{ cm}^{-2}$ at about 24arcsec from Sgr A* with a beam of about 30arcmin. This is also lower than the hydrogen column density of $1.1 \times 10^{23} \text{ cm}^{-2}$ determined by Russell et al. (2017) with their five colliding wind models since we separated the ISM and local components of N_{H} .

The hydrogen column density of the ISM is related to the optical extinction A_V (at $0.55\mu\text{m}$) of the observed objects. Regarding the optical extinction towards the Galac-

Table 1. Results of the MCMC fitting of spectra of the X-ray diffuse emission from the Galactic Centre.

Region	Area (arcsec ²)	$N_{\text{H,local}}$ (10^{22} cm ⁻²)	κT_1 (keV)	N_1 (10^{-5} cm ⁻³ arcsec ⁻²)	κT_2 (keV)	N_2 (10^{-6} cm ⁻³ arcsec ⁻²)	n_{C}	n_{S}	n_{Ar}	n_{Ca}	n_{Fe}	χ^2
1.5–5.4 arcsec	67.9	$9.6^{+0.3}_{-0.4}$	$1.05^{+0.08}_{-0.07}$	$8.9^{+1.5}_{-1.2}$	$4.6^{+0.6}_{-0.5}$	$10.5^{+1.7}_{-1.6}$	$0.89^{+0.08}_{-0.06}$	$1.07^{+0.09}_{-0.09}$	$1.3^{+0.2}_{-0.2}$	$1.9^{+0.2}_{-0.2}$	$0.62^{+0.04}_{-0.04}$	300/222
5.4–9.2 arcsec	137.4	$10.0^{+0.4}_{-0.5}$	$0.91^{+0.06}_{-0.06}$	$6.4^{+1.1}_{-0.9}$	$4.8^{+0.5}_{-0.5}$	$6.2^{+0.7}_{-0.8}$	—	—	—	—	—	304/226
9.2–13.1 arcsec	190.8	$8.4^{+0.5}_{-0.5}$	$0.76^{+0.07}_{-0.07}$	$4.7^{+1.3}_{-1.0}$	$3.4^{+0.3}_{-0.3}$	$6.3^{+0.9}_{-0.7}$	—	—	—	—	—	281/222
13.1–17 arcsec	228.5	$9.9^{+0.3}_{-0.4}$	$0.41^{+0.03}_{-0.03}$	137^{+54}_{-46}	$2.7^{+0.3}_{-0.2}$	$10.2^{+1.1}_{-1.4}$	—	—	—	—	—	319/191
CND	4574.8	$2.3^{+0.8}_{-0.4}$	$1.80^{+0.03}_{-0.03}$	$0.99^{+0.05}_{-0.05}$	$0.07^{+0.05}_{-0.05}$	$1.12^{+0.06}_{-0.06}$	$0.7^{+0.1}_{-0.1}$	$0.65^{+0.08}_{-0.07}$	$6.8^{+1.6}_{-1.3}$	774/570
“Outside”	2005.7	$3.9^{+0.4}_{-0.4}$	$0.35^{+0.02}_{-0.02}$	$0.03^{+0.01}_{-0.01}$	$1.30^{+0.04}_{-0.03}$	$17.1^{+1.4}_{-1.8}$	$1.0^{+0.1}_{-0.1}$	$1.6^{+0.2}_{-0.2}$	$1.3^{+0.2}_{-0.2}$	$2.3^{+0.3}_{-0.2}$	$5.9^{+0.3}_{-0.4}$	1376/456

Notes: Best-fitting parameters for the simultaneous fitting of the twelve src+bkg spectra, considering the bkg spectrum extracted from the bkg region 2, with the `pileup*dustscat*TBnew*vphabs*(VAPEC+VAPEC)` model. ^(a) The local hydrogen column density describing the self-absorption by the local gas in the different regions. ^(b) The temperatures of the two APEC models. ^(c) The normalization parameters of the two APEC models. ^(d) Abundance of metals.

tic Centre, several studies have already been made (e.g. Rieke et al. 1989; Cardelli et al. 1989). Fritz et al. (2011) compiled the extinctions measured by six previous studies towards the inner 14 arcsec \times 20 arcsec of the Galactic Centre. They pointed out a large discrepancy between the values of the optical extinctions derived from observations at different wavelengths. The values span from $A_V = 31$ mag when using the NIR images to $A_V = 56.7$ mag when using the hydrogen column density deduced from the X-ray flare spectra. The higher values deduced from the X-ray studies are probably due to an incorrect usage of the relation given by Predehl & Schmitt (1995) between the hydrogen column density and the optical extinction. Indeed, the hydrogen column densities used by Predehl & Schmitt (1995) were computed using the Morrison & McCammon (1983)’s cross sections for photoelectric absorption and the Anders & Ebihara (1982)’s abundances. However, these cross sections and abundances were updated by Verner et al. (1996) and Wilms et al. (2000), respectively, leading to a hydrogen column density which is 1.5 times lower than previously obtained by Predehl & Schmitt (1995). The corrected Predehl & Schmitt (1995)’s relation that has to be used when utilizing the Verner et al. (1996)’s cross sections and Wilms et al. (2000)’s abundances is thus $N_{\text{H}}/A_V = 2.69 \times 10^{21} \text{ cm}^{-2} \text{ mag}^{-1}$ as already mentioned by Nowak et al. (2012). Using this relation and the $N_{\text{H,ISM}}$ obtained here, we deduced an optical extinction of $A_V = 27.9^{+0.7}_{-1.5}$ mag. This is certainly well below the values deduced from the previous X-ray studies. Our value is close but larger than $A_V = 25$ mag found from stellar colours by Schödel et al. (2010) for central few arcseconds surrounding the position of Sgr A*. This is even much closer to the typical extinction of about 30 mag averaged in the central parsec (Rieke et al. 1989 and see values summarized in the introduction by Schödel et al. 2010) since we derived the extinction value as an average from a large region of about 100 arcsec.

The best-fitting parameters for the local hydrogen column density is almost constant for the innermost regions (i.e., below 17 arcsec) with a mean value of about $9.5 \times 10^{22} \text{ cm}^{-2}$. The Galactic Centre environment is thus responsible for about one third of the absorption of the X-rays because of the higher metallicity compared to the Galactic arms. Even if the values of the $N_{\text{H,local}}$ below 17 arcsec are consistent within the uncertainties, they have large variations around the mean with a standard deviation of $0.7 \times 10^{22} \text{ cm}^{-2}$. This behaviour reflects the inhomogeneities in the density of the gas in the Galactic Centre. The local hydrogen column density in the CND region is 4.1 times smaller than

those measured below 17 arcsec while in the region “outside” the CND, the local hydrogen column density is 2.4 times smaller than those measured below 17 arcsec (see upper panel of Fig. 4).

5.2 Relative abundances

The abundances of C, S, Ar and Ca in the “outside” region are comparable to those observed below 17 arcsec. However, these abundances are very different in the CND region. Moreover, the abundances of Fe in the CND region and the “outside” region, are about 10 times those in the inner regions. The study of the spatial distribution of the Fe XXV K_{β} line shows that the bulk of the emission is located towards the North-East of Sgr A*. This high Fe abundance is now well explained by the reversed shock-heated ejecta of the Sgr A East supernova remnant (Maeda et al. 2002; Park et al. 2005; Lau et al. 2015). What is important to note is the critical change of Fe abundance close to the inner part of the CND due to a drastic change in the nature of the emitting plasma between the central region and the CND.

This change was already mentioned by Lau et al. (2015) who deduced a change of the plasma heating mechanism when studying the mid-infrared colour maps. These authors argued that the interior of the supernova remnant is predominantly heating by the radiation field from the central stellar cluster. The dominance of this heating process was also mentioned by Baganoff et al. (2003) who pointed out an enhanced X-ray emission in individual stellar aggregates close to Sgr A* like the IRS13E cluster and the overall IRS16 cluster which contain He-stars which have surface temperatures of up to 30000 K resulting in strong and fast (up to 1000 km s^{-1}) stellar winds that blow huge mass-loss rates (e.g., Najarro et al. 1997). In addition, the activity of the central regions is underlined by the presence of two extended X-ray lobes (Markoff 2010) apparently created by the hot X-ray luminous gas originating from within the central parsec and most likely from within the CND. All of these facts show that the central stellar cluster in combination with Sgr A* are a dominant heating source within the central regions. We confirmed here, thanks to the X-ray data, that the non-thermal emission of the shocked ejecta of the supernova remnant is negligible in the spectra from the central regions since there is no hint of this radiative process.

The higher iron abundance in the CND and the “outside” regions should implies a larger absorption by photoionization of the X-rays which is in contradiction with the decay of the hydrogen column densities in these regions pre-

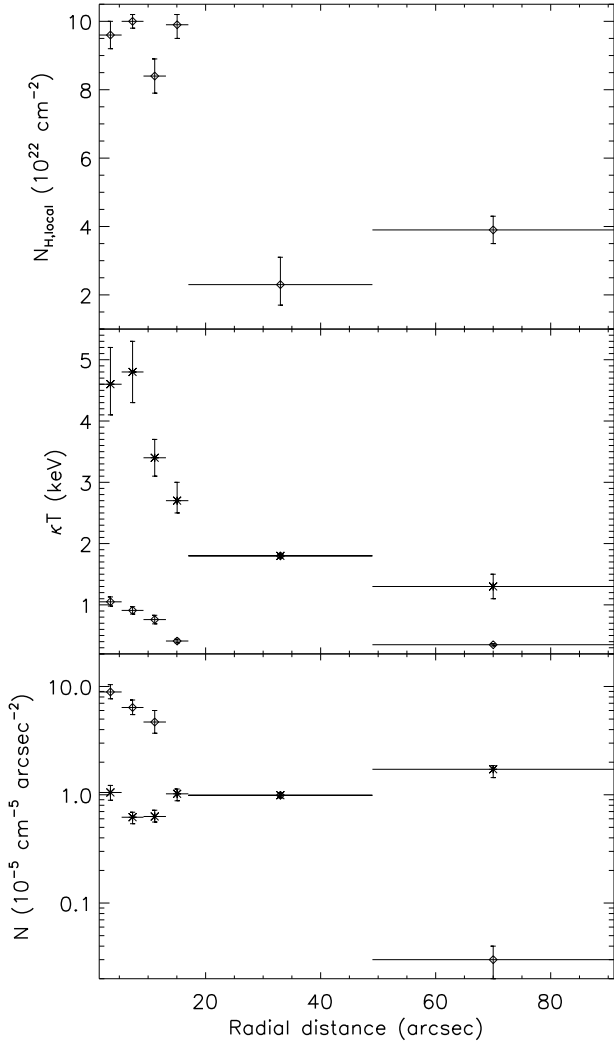


Figure 4. Evolution of hydrogen column density, temperature and normalization parameter of the APEC model with radial distance from Sgr A*. *Top panel:* The evolution of hydrogen column density and its error bars. The horizontal lines show the extend of the spectral extraction region. *Middle panel:* The evolution of the plasma temperature. The asterisks and diamonds show the temperature of the hard and soft plasma, respectively. *Bottom panel:* The evolution of the normalization of the APEC spectral model. The asterisks and diamonds show the normalization of the hard and soft plasma, respectively.

sented in the previous subsection. This is an additional clue to argue that the plasma constituting the CND and the outside region is not “simply” the same plasma as in the central regions which is more absorbed but a physically different plasma characterized by its own physical characteristics and its own absorption.

5.3 Electron temperature

As already shown in Markoff (2010), the plasma is well described by two temperatures: a soft component with a temperature around 0.8 keV and a hard component with a temperature of a few keV.

The electron temperature of the soft plasma decreases

with the radial distance from 1.5 to 17 arcsec with a mean value of 0.8 keV (about 8×10^6 K). Fitting the temperature distribution of the soft plasma with the radial distance r from Sgr A* for r between 1.5 and 17 arcsec with $\kappa T = br^a$, we obtain $a = -0.57 \pm 0.06$ and $b = 2.4 \pm 0.1$ keV. Extrapolating this curve until the region of the CND and “outside” the CND, the derived temperatures are 0.3 and 0.2 keV which is well below the best-fitting value of the spectra, especially for the CND region. There is thus a change of the soft plasma characteristics at around 17 arcsec from Sgr A*.

Fitting the temperature distribution of the hard plasma in the inner 17 arcsec as above, we obtained $a = -0.39 \pm 0.09$ and $b = 8.5 \pm 0.2$ keV. Extrapolating this curve until the region of the CND and “outside” the CND, the derived temperatures are 2.2 and 1.6 keV which is well above the best-fitting value of the spectrum. There is thus also a change of the hard plasma characteristics at around 17 arcsec from Sgr A*.

Moreover, the CND plasma is characterized by a 1T plasma instead of a 2T plasma.

The drastic change of the temperature in the CND region is an additional hint showing that this plasma is physically different than the plasma in the innermost region.

5.4 The CND: a barrier for the central plasma

From these comparisons of the plasma characteristics, we deduced that the plasma in the innermost regions is very different from those of the CND region: in the latter, the plasma is characterized by only one temperature and the relative abundances of iron and the local hydrogen column density are 10 and 4 times lower in the central regions, respectively. This last characteristic definitely rules out the hypothesis according to which the CND acts as an absorbing material for the background X-ray diffuse emission. The CND thus rather acts as a boundary for the central plasma. This interpretation was already suggested by Baganoff et al. (2003) and Rockefeller et al. (2004) but is confirmed here thanks to the X-ray observations of the Galactic Centre.

The physical characteristics of the “outside” region are also different from those of the CND: in the former region, the plasma is well described by two temperatures and the abundances are larger except for the Fe. This implies that the plasma in the CND region is also different to those of the “outside” region. This extension of the plasma towards the North-East region may correspond to the collimated outflow created by a jet-like structure related to Sgr A* or by the interaction between the mass-loss of massive stars and the mini-spiral material as presented by Mužić et al. (2007) to explain the motions of thin dust filaments at the Galactic Centre.

This scenario (represented in Fig. 5) may confirm one of the hypothesis of Markoff (2010) which explained the X-ray lobes observed symmetrically around Sgr A* at large distance (about 30 pc) thanks to the collimator role of the CND which blocks the plasma expansion in the Galactic plane direction and ejects it in the perpendicular direction.

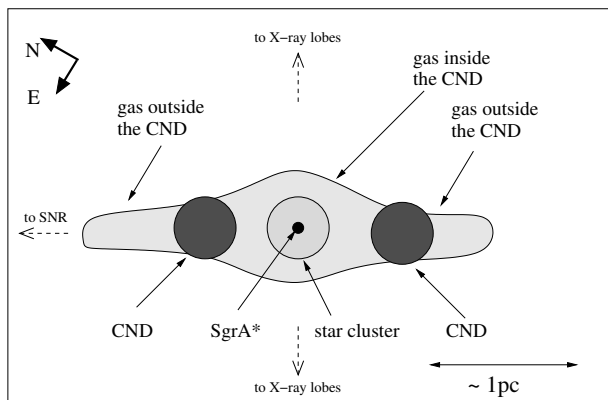


Figure 5. Vertical cut through the Galactic Centre showing some individual components. The scale is approximate. The dashed arrows point towards the SNR to the North-East and to the X-ray lobes extending a few arc-minute above and below the Galactic plane (Markoff 2010). Both of these structures are not contained in this sketch.

6 CONCLUSION

The knowledge on the distribution of the hot ionized and cold molecular gas phases in the Galactic Centre is essential to understand the interplay between radiative cooling, star formation and feedback processes in that turbulent region (Souza Lima et al. 2017). The presence of complex molecular tracers in individual sections of the CircumNuclear disk (CND) indicates high densities and low temperatures (Moser et al. 2017; Christopher et al. 2005), i.e., ideal conditions for star formations (Yusef-Zadeh et al. 2017; Jalali et al. 2014). Although at the Galactic Centre the effects of the central stellar cluster and the hot ionized gas are presently much weaker than it apparently is in the case of active galactic nuclei, these components may have an important impact on the CND’s activity cycle (Blank et al. 2016).

Thanks to thirteen years of observations with Chandra, we detected, for the first time, the depression of the X-ray luminosity in a region whose the size and location corresponds to the CND which was already observed in emission in radio and far-infrared.

Using the MCMC method, we compared the plasma characteristics in the innermost regions (i.e., between 1.5 and 17arcsec), in the CND (i.e., between 17arcsec and 49arcsec) and at the North-East outside the CND. A sketch of the individual components is shown in Fig. 5.

The X-ray emission of the plasma is absorbed by two components: the hydrogen column density of the ISM and the local hydrogen column density at the Galactic Centre. The hydrogen column density of the ISM is about $7.5^{+0.2}_{-0.4} \times 10^{22} \text{ cm}^{-2}$. Using the corrected relation of Predehl & Schmitt (1995), $N_{\text{H}}/A_{\text{V}} = 2.69 \times 10^{21} \text{ cm}^{-2} \text{ mag}^{-1}$, the deduced an optical extinction of $A_{\text{V}} = 27.9^{+0.7}_{-1.5} \text{ mag}$.

We showed that the spectra of the X-ray diffuse emission from the central parsec of the Galactic Centre is well described by a two-temperature plasma. The local hydrogen column density is responsible for one third of the total X-rays absorption along the line-of-sight because of the large metal abundance of the Galactic bulge compared to the spiral arms. We also confirmed that the central regions are pre-

dominantly heated via the radiation field from the central stellar cluster.

In the CND region, the plasma is better represented by a one temperature plasma of 1.8keV and the local hydrogen column density is lower than in the innermost regions. The depression behaviour of the X-ray luminosity is thus likely due to a less effective heating of the plasma compared to below 17arcsec and not to a higher absorption. Since we do not know the exact 3D shape of the different regions, it is difficult to determine if the decay of hydrogen column density in the CND is due to a lower scale height or a decay of the density. For illustrative purpose, we assume in Fig. 5 that the scale height of the hot gas in the innermost regions is larger than inside or outside the CND. We also showed that the CND rather acts as a barrier for the central plasma.

The high iron abundance of the plasma in the CND and the “outside” region confirms that these regions are dominated by the shock-heated ejecta of the Sgr A East supernova remnant.

Finally, the plasma extension outside the CND in the North-East region may correspond to the collimated outflow created by the mass-losing stars and possibly Sgr A* and presented by Mužić et al. (2007) to explain the motions of thin dust filaments at the Galactic Centre.

ACKNOWLEDGEMENTS

This work was supported by Deutsche Forschungsgemeinschaft (DFG) funded CRC 956 - Conditions and Impact of Star Formation, the University of Cologne, and the European Union Seventh Framework Program (FP7/2007-2013) under grant agreement No. 312789, Strong Gravity: Probing Strong Gravity by Black Holes Across the Range of Masses. This work has also been discussed in the framework of the Deutsche Forschungsgemeinschaft (DFG) SFB 956: Conditions and Impact of Star Formation. This work is based on public data obtained from the Chandra Data Archive. We thank the PIs that obtained since 1999 the X-ray observations of Sgr A* used in this work.

REFERENCES

- Anders E., Ebihara M., 1982, *Geochimica Cosmochimica Acta*, **46**, 2363
- Baganoff F. K., et al., 2003, *ApJ*, **591**, 891
- Blank M., Morris M. R., Frank A., Carroll-Nellenback J. J., Duschl W. J., 2016, *MNRAS*, **459**, 1721
- Cardelli J. A., Clayton G. C., Mathis J. S., 1989, *ApJ*, **345**, 245
- Christopher M. H., Scoville N. Z., Stolovy S. R., Yun M. S., 2005, *ApJ*, **622**, 346
- Davis J. E., 2001, *ApJ*, **562**, 575
- Degenaar N., Reynolds M. T., Wijnands R., Miller J. M., Kennea J. A., Ponti G., Haggard D., Gehrels N., 2016, *The Astronomer’s Telegram*, **9109**
- Dwelly T., Ponti G., 2013, *The Astronomer’s Telegram*, **5008**, 1
- Eckart A., Genzel R., 1999, in Ossenkopf V., Stutzki J., Winnewisser G., eds, *The Physics and Chemistry of the Interstellar Medium*.
- Ekers R. D., van Gorkom J. H., Schwarz U. J., Goss W. M., 1983, *A&A*, **122**, 143
- Falcke H., Markoff S. B., 2013, *Classical and Quantum Gravity*, **30**, 244003

- Foreman-Mackey D., Hogg D. W., Lang D., Goodman J., 2013, *PASP*, **125**, 306
- Freeman P. E., Kashyap V., Rosner R., Lamb D. Q., 2002, *ApJS*, **138**, 185
- Fritz T. K., et al., 2011, *ApJ*, **737**, 73
- Garmire G. P., Bautz M. W., Ford P. G., Nousek J. A., Ricker Jr. G. R., 2003, in Truemper J. E., Tananbaum H. D., eds, Society of Photo-Optical Instrumentation Engineers (SPIE) Conference Series Vol. 4851, X-Ray and Gamma-Ray Telescopes and Instruments for Astronomy.. pp 28–44, doi:10.1117/12.461599
- Gehrels N., et al., 2013, The Astronomer’s Telegram, **5037**, 1
- Gelman A., Roberts G., Gilks W., 1996, Efficient Metropolis jumping rules. Oxford University Press
- Genzel R., Schödel R., Ott T., Eckart A., Alexander T., Lacombe F., Rouan D., Aschenbach B., 2003, *Nature*, **425**, 934
- Genzel R., Eisenhauer F., Gillessen S., 2010, *Reviews of Modern Physics*, **82**, 3121
- Ghez A. M., et al., 2008, *ApJ*, **689**, 1044
- Gillessen S., Eisenhauer F., Fritz T. K., Bartko H., Dodds-Eden K., Pfuhl O., Ott T., Genzel R., 2009, *ApJ*, **707**, L114
- Goodman J., Weare J., 2010, *Communications in Applied Mathematics and Computational Science*, **5**, 65
- Herrnstein R. M., Ho P. T. P., 2005, *ApJ*, **620**, 287
- Jalali B., et al., 2014, *MNRAS*, **444**, 1205
- Kalberla P. M. W., Burton W. B., Hartmann D., Arnal E. M., Bajaja E., Morras R., Pöppel W. G. L., 2005, *A&A*, **440**, 775
- Kennea J. A., et al., 2013, *ApJ*, **770**, L24
- Krabbe A., Genzel R., Drapatz S., Rotaciuc V., 1991, *ApJ*, **382**, L19
- Lau R. M., Herter T. L., Morris M. R., Becklin E. E., Adams J. D., 2013, *ApJ*, **775**, 37
- Lau R. M., Herter T. L., Morris M. R., Li Z., Adams J. D., 2015, *Science*, **348**, 413
- Li Z., Morris M. R., Baganoff F. K., 2013, *ApJ*, **779**, 154
- Maeda Y., et al., 2002, *ApJ*, **570**, 671
- Markoff S., 2010, *Proceedings of the National Academy of Science*, **107**, 7196
- Martín S., Martín-Pintado J., Montero-Castaño M., Ho P. T. P., Blundell R., 2012, *A&A*, **539**, A29
- Masui K., Mitsuda K., Yamasaki N. Y., Takei Y., Kimura S., Yoshino T., McCammon D., 2009, *PASJ*, **61**, S115
- Moorwood A., et al., 1998, *The Messenger*, **94**, 7
- Morrison R., McCammon D., 1983, *ApJ*, **270**, 119
- Moser L., et al., 2017, *A&A*, **603**, A68
- Muno M. P., et al., 2003, *ApJ*, **589**, 225
- Muno M. P., et al., 2004, *ApJ*, **613**, 326
- Mužić K., Eckart A., Schödel R., Meyer L., Zensus A., 2007, *A&A*, **469**, 993
- Najarro F., Krabbe A., Genzel R., Lutz D., Kudritzki R. P., Hillier D. J., 1997, *A&A*, **325**, 700
- Neilsen J., et al., 2013, *ApJ*, **774**, 42
- Nishiyama S., Schödel R., 2013, *A&A*, **549**, A57
- Nowak M. A., et al., 2012, *ApJ*, **759**, 95
- Park S., et al., 2005, *ApJ*, **631**, 964
- Petrov L., Kovalev Y. Y., Fomalont E. B., Gordon D., 2011, *AJ*, **142**, 35
- Predehl P., Schmitt J. H. M. M., 1995, *A&A*, **293**, 889
- Quataert E., 2004, *ApJ*, **613**, 322
- Raymond J. C., Smith B. W., 1977, *ApJS*, **35**, 419
- Reynolds M., Kennea J., Degenaar N., Wijnands R., Miller J., 2016, The Astronomer’s Telegram, **8649**
- Rieke G. H., Rieke M. J., Paul A. E., 1989, *ApJ*, **336**, 752
- Rockefeller G., Fryer C. L., Melia F., Warren M. S., 2004, *ApJ*, **604**, 662
- Russell C. M. P., Wang Q. D., Cuadra J., 2017, *MNRAS*, **464**, 4958
- Sakano M., Warwick R. S., Decourchelle A., Predehl P., 2004, *MNRAS*, **350**, 129
- Schödel R., et al., 2002, *Nature*, **419**, 694
- Schödel R., Najarro F., Muzic K., Eckart A., 2010, *A&A*, **511**, A18
- Sjouwerman L. O., Pihlström Y. M., 2008, *ApJ*, **681**, 1287
- Smith R. K., Brickhouse N. S., Liedahl D. A., Raymond J. C., 2001, *ApJ*, **556**, L91
- Souza Lima R., Mayer L., Capelo P. R., Bellovary J. M., 2017, *ApJ*, **838**, 13
- Verner D. A., Ferland G. J., Korista K. T., Yakovlev D. G., 1996, *ApJ*, **465**, 487
- Wang Q. D., Lu F. J., Gotthelf E. V., 2006, *MNRAS*, **367**, 937
- Wang Q. D., et al., 2013, *Science*, **341**, 981
- Wilms J., Allen A., McCray R., 2000, *ApJ*, **542**, 914
- Yuan F., Narayan R., 2014, *ARA&A*, **52**, 529
- Yuan F., Quataert E., Narayan R., 2003, *ApJ*, **598**, 301
- Yusef-Zadeh F., Cotton W., Wardle M., Royster M. J., Kunneriath D., Roberts D. A., Wootten A., Schödel R., 2017, *MNRAS*,

APPENDIX A: THE BEST-FITTING MODELS FOR THE SPECTRA OF THE X-RAY DIFFUSE EMISSION

In Figures A1 to A10, we show the results of the Markov Chain Monte Carlo (MCMC) fitting of the twelve spectra from the Galactic Centre. The marginal distributions in the diagonal plots are the histograms of the values taken by all walkers at each step after the “burn-in” period. The joint distributions between each couple of parameters are shown in the other plots with the confidence levels at 68, 90 and 99%. The best fitting parameters, defined by the median of the marginal distributions, are shown by the dot-dashed line in the marginal distributions and by a cross in the joint distributions. We only show here the joint distributions between the parameters which are physically meaningful. Figure A1 represents the local and ISM hydrogen column densities. Figures A2, A3 and A4 represent the abundances of the inner regions, the CND region and the “outside” region, respectively. Figures A5 to A10 represent the plasma characteristics of each of the six regions. Finally, Fig. A11 shows the twelve spectra and the best fitting models.

APPENDIX B: THE MODELS FOR THE SPATIAL DISTRIBUTION OF THE X-RAY DIFFUSE EMISSION

In Fig. 1 we have used our preferred model of the X-ray emission that accounts for a first order description of the extended X-ray emission towards the Galactic Centre including the emission in the immediate vicinity (i.e., the central arc-minute) of Sgr A* and the emission from the SNR to the North-East of the centre. In order to demonstrate that the result of the applied algorithm to extract the rings structure is not strongly dependent on the used model for the extended emission as long as it is sufficiently flat across the central arc-minute we show in Fig. B1 modelling results from a variety of assumed X-ray distributions. In size and structure all of these models are in significantly worse agreement with the observed overall structure of the extended emission reveal the main structural features of the shadow. In model 1, model 2, and model 3 we use a circular Gaussian with a FWHM of 100arcsec, 300arcsec, and 150arcsec,

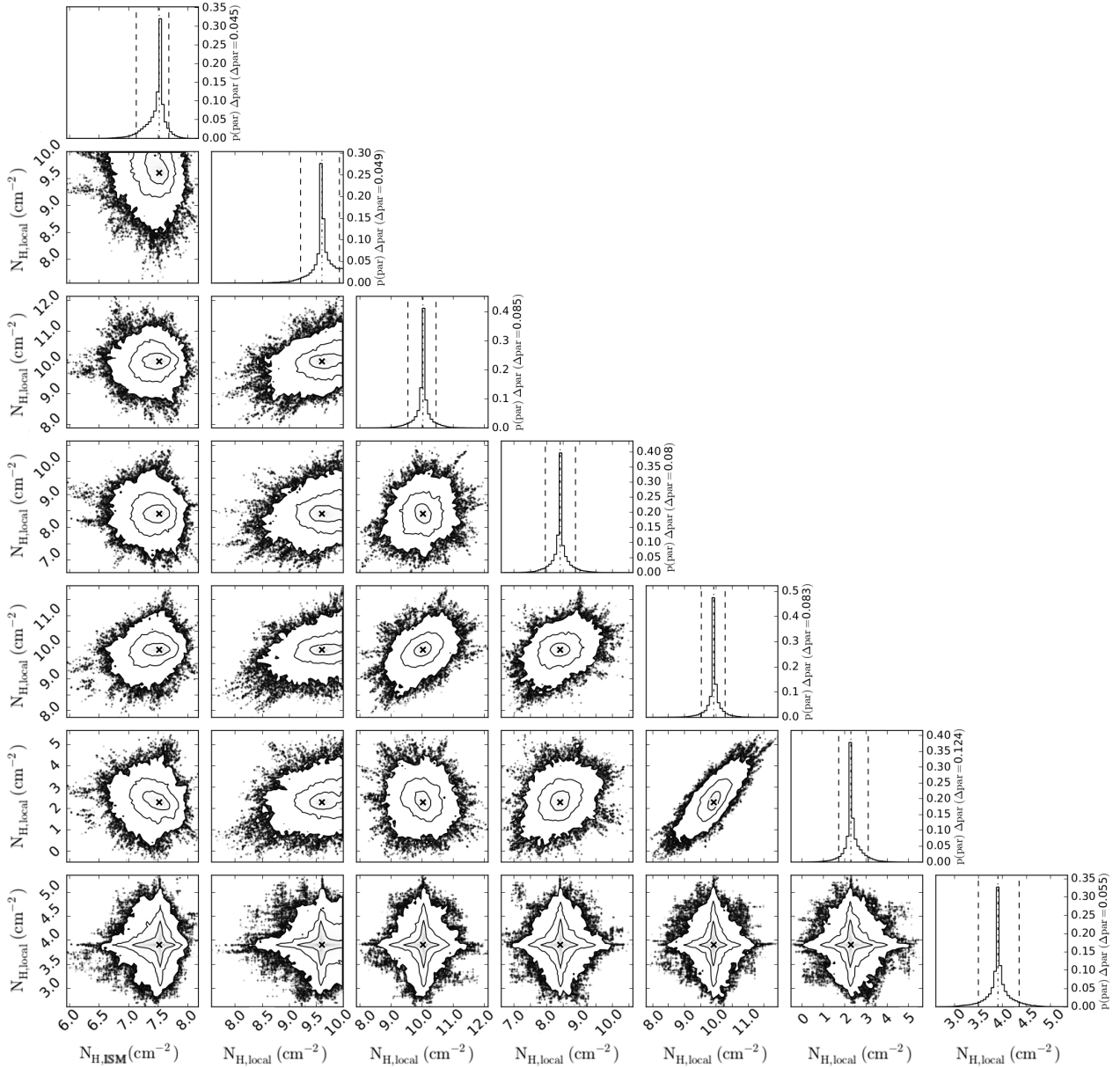


Figure A1. Triangle plot of the of the hydrogen column density values taken by the walkers during the MCMC fitting after the “burn-in” period. The diagonal plots are the marginal distribution. The dot-dashed lines in these plots are the best-fitting parameter determined as the median of the marginal distribution. The dotted lines determine the 90% confidence range, i.e., between the 5th and 95th percentile of the marginal distribution. The other plots are the joint distribution between two parameters. The cross in these plots are the best-fitting parameters. The ISM hydrogen column density is shown in the left column whereas the local hydrogen column densities of the 1.5–5.4arcsec, 5.4–9.2arcsec, 9.2–13.1arcsec, 13.1–17arcsec, CND and “outside” regions are shown in the following columns.

respectively. All the three models have higher fluxes above and below the Galactic Plane, hence, the ring features in this direction are over-represented in these directions. The models exhibit too little flux in the direction of the SNR, hence, the ring structure is under-represented with respect to our preferred model in Fig. 1. Other than that, the overall ring structure including the locations of strongest extinction are represented well, independent of the model assumptions.

This paper has been typeset from a $\text{\TeX}/\text{\LaTeX}$ file prepared by the author.

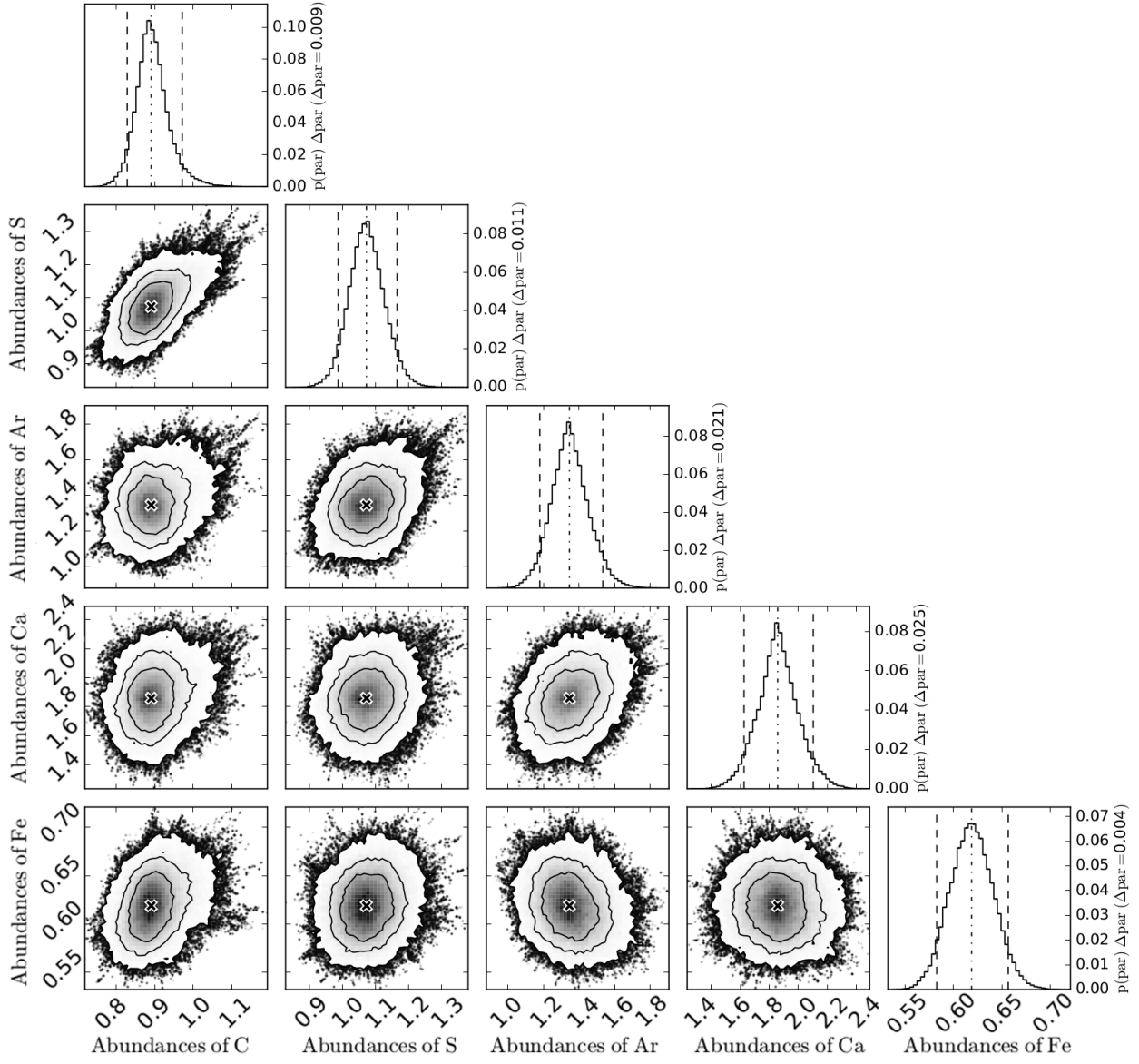


Figure A2. Triangle plot of the relative abundances below 17arcsec. See caption of Fig. A1 for details.

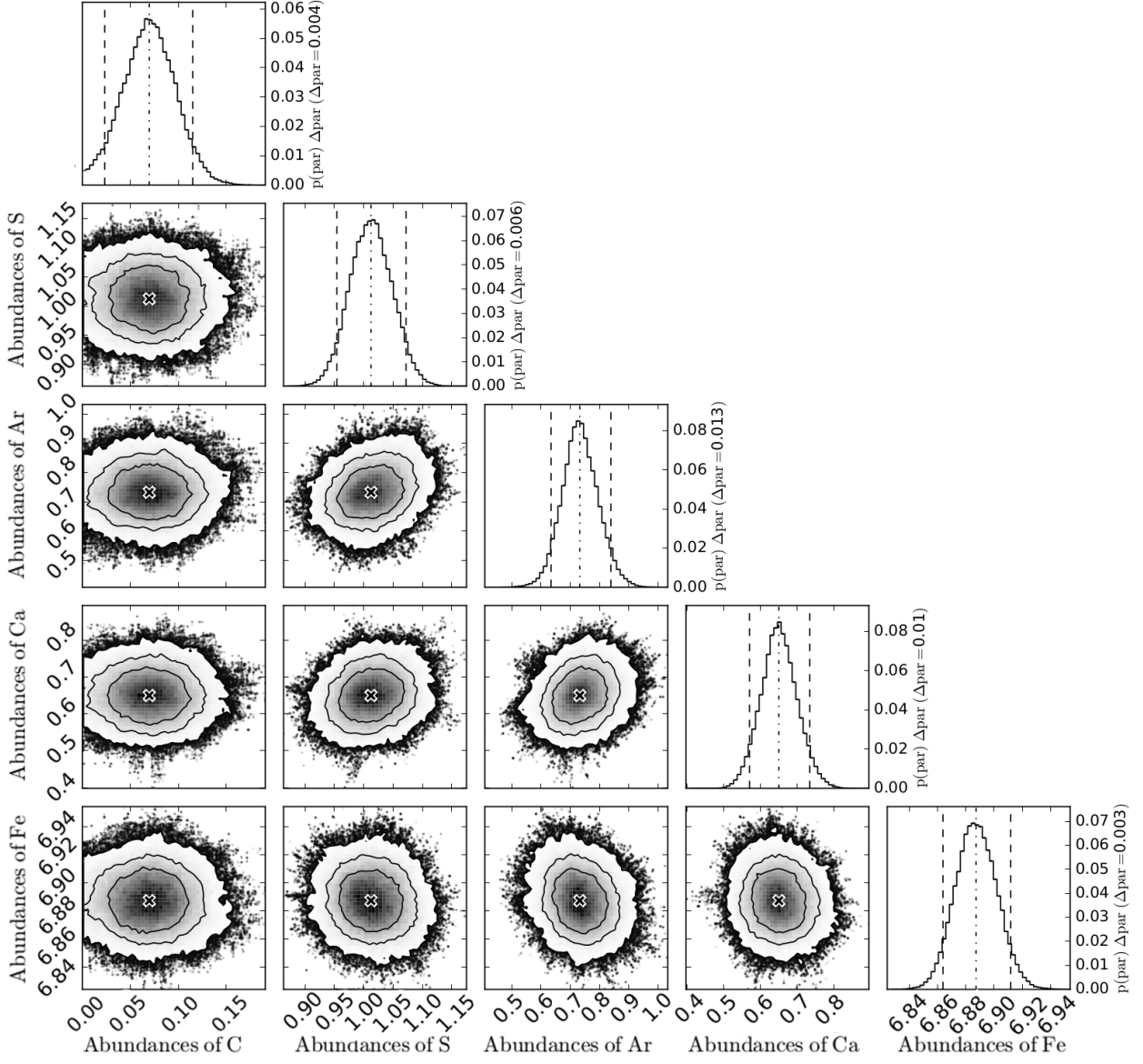


Figure A3. Triangle plot of the relative abundances in the CND region. See caption of Fig. A1 for details.

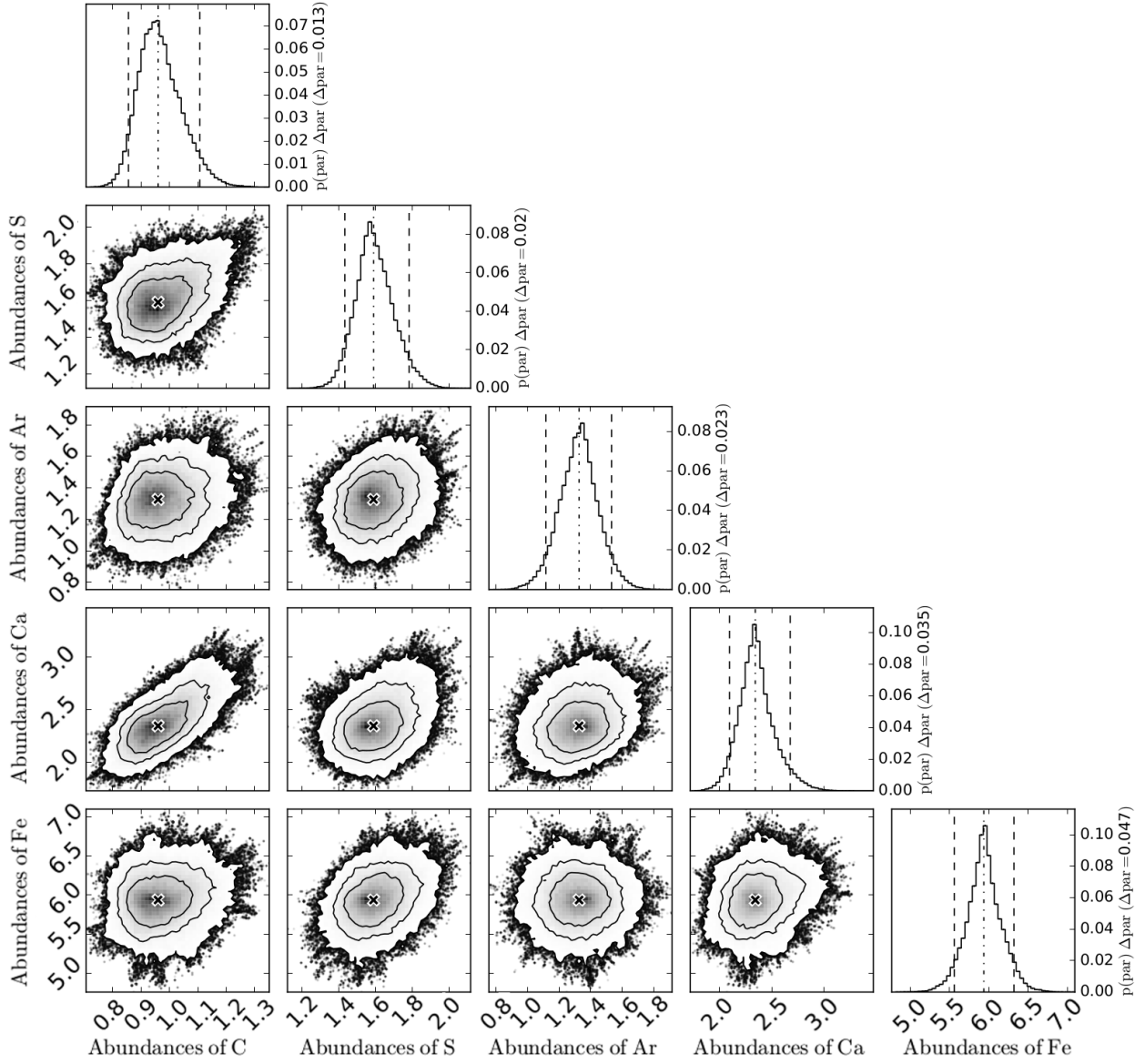


Figure A4. Triangle plot of the relative abundances “outside” the CND. See caption of Fig. A1 for details.

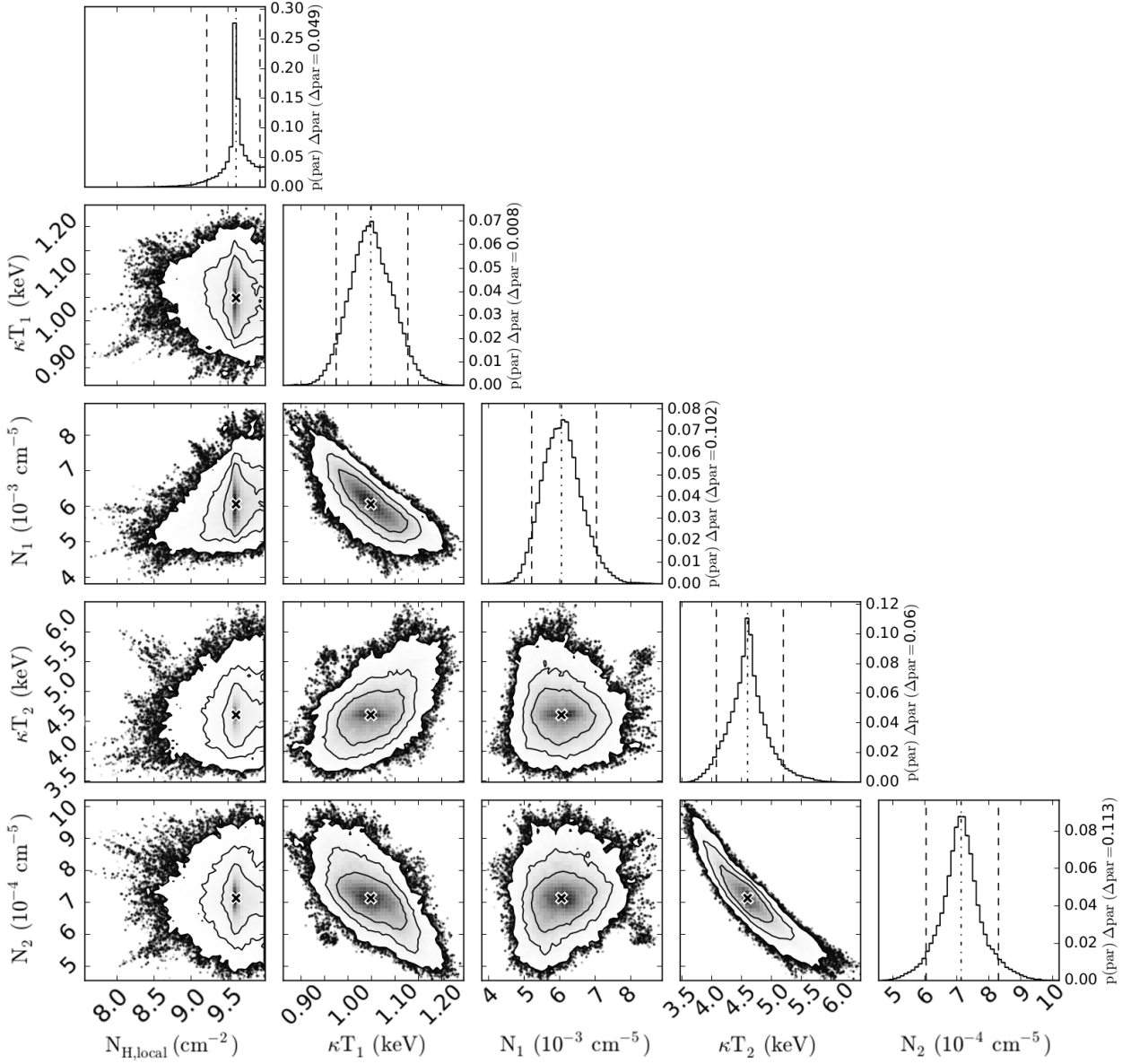


Figure A5. Triangle plot of the local hydrogen column density, the two temperatures and normalization parameters of the 1.5–5.4arcsec region. See caption of Fig. A1 for details. Note that the normalization parameters are not normalized by the extraction region area contrarily to those reported in Table 1.

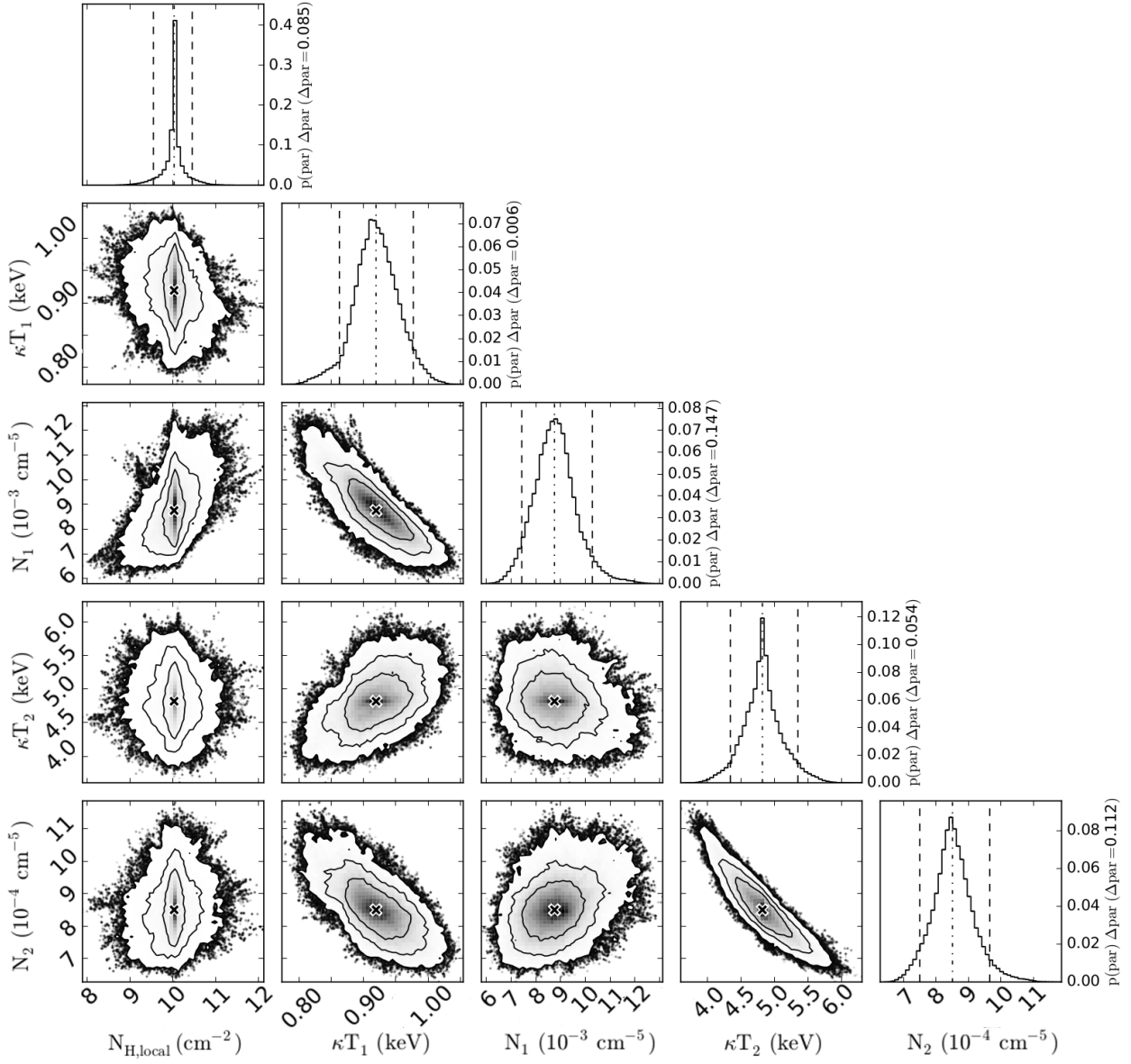


Figure A6. Triangle plot of the local hydrogen column density, the two temperatures and normalization parameters of the 5.4–9.2arcsec region. See caption of Fig. A1 for details. Note that the normalization parameters are not normalized by the extraction region area contrarily to those reported in Table 1.

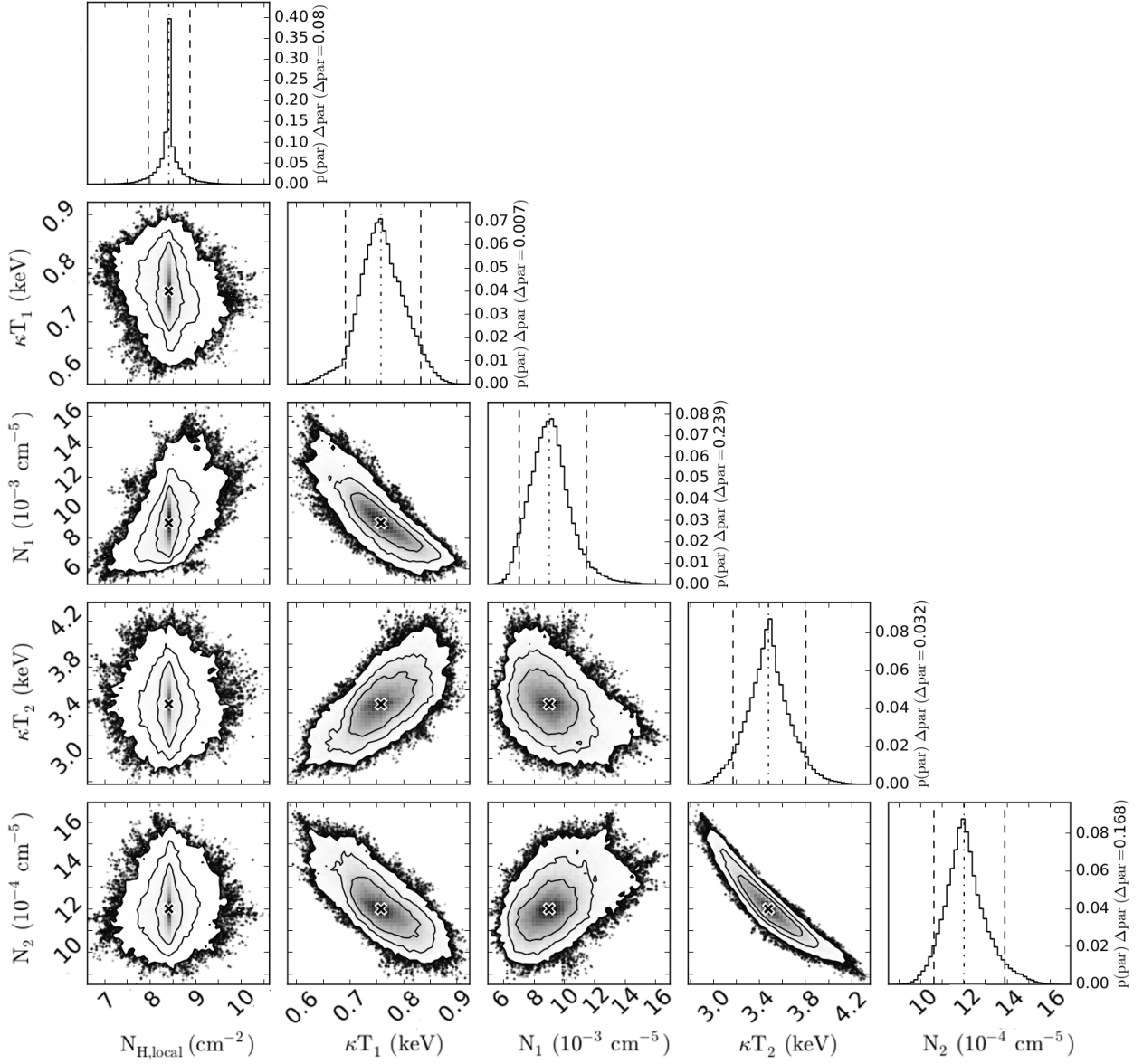


Figure A7. Triangle plot of the local hydrogen column density, the two temperatures and normalization parameters of the 9.2–13.1 arcsec region. See caption of Fig. A1 for details. Note that the normalization parameters are not normalized by the extraction region area contrarily to those reported in Table 1.

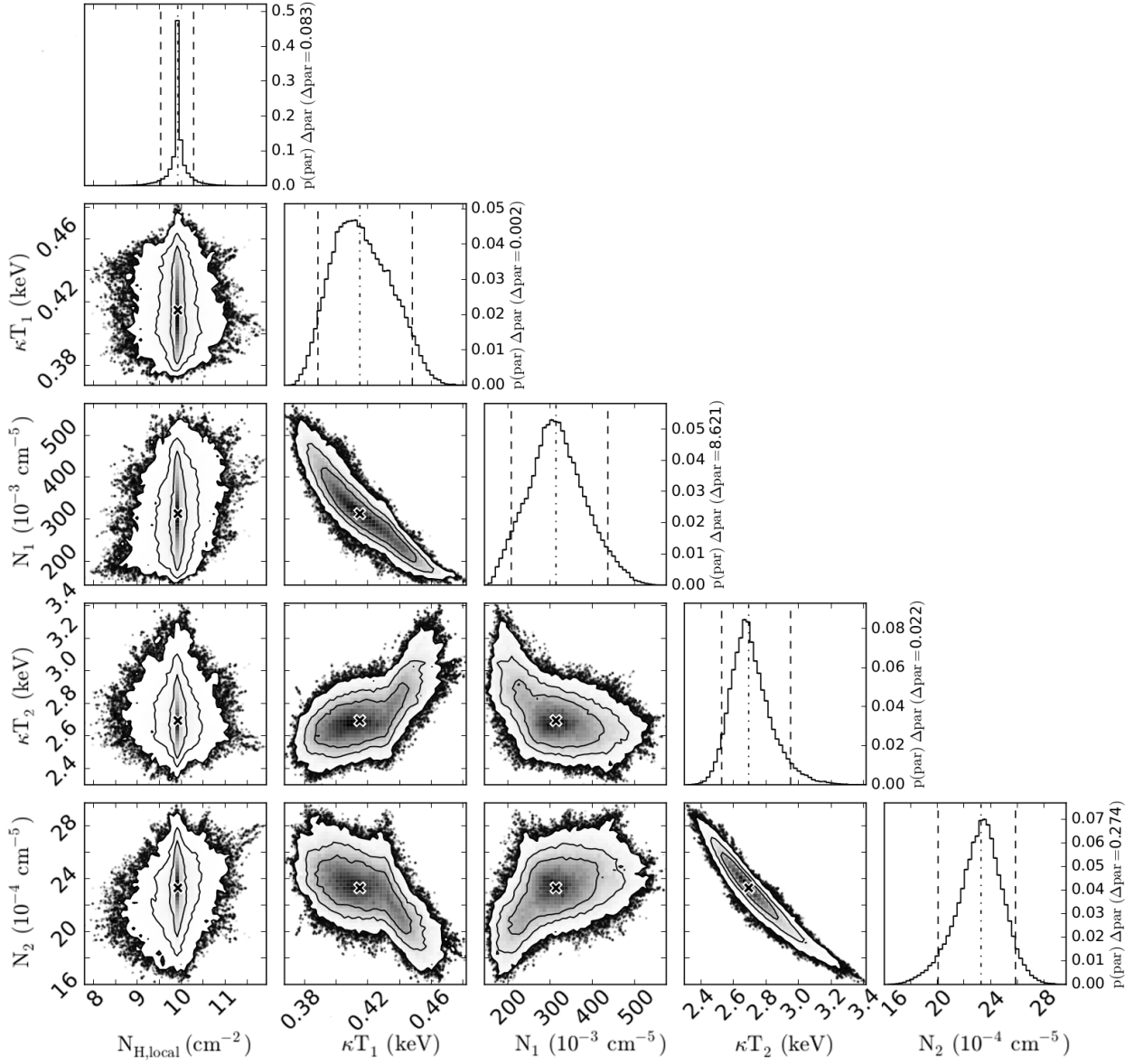


Figure A8. Triangle plot of the local hydrogen column density, the two temperatures and normalization parameters of the 13.1–17arcsec region. See caption of Fig. A1 for details. Note that the normalization parameters are not normalized by the extraction region area contrarily to those reported in Table 1.

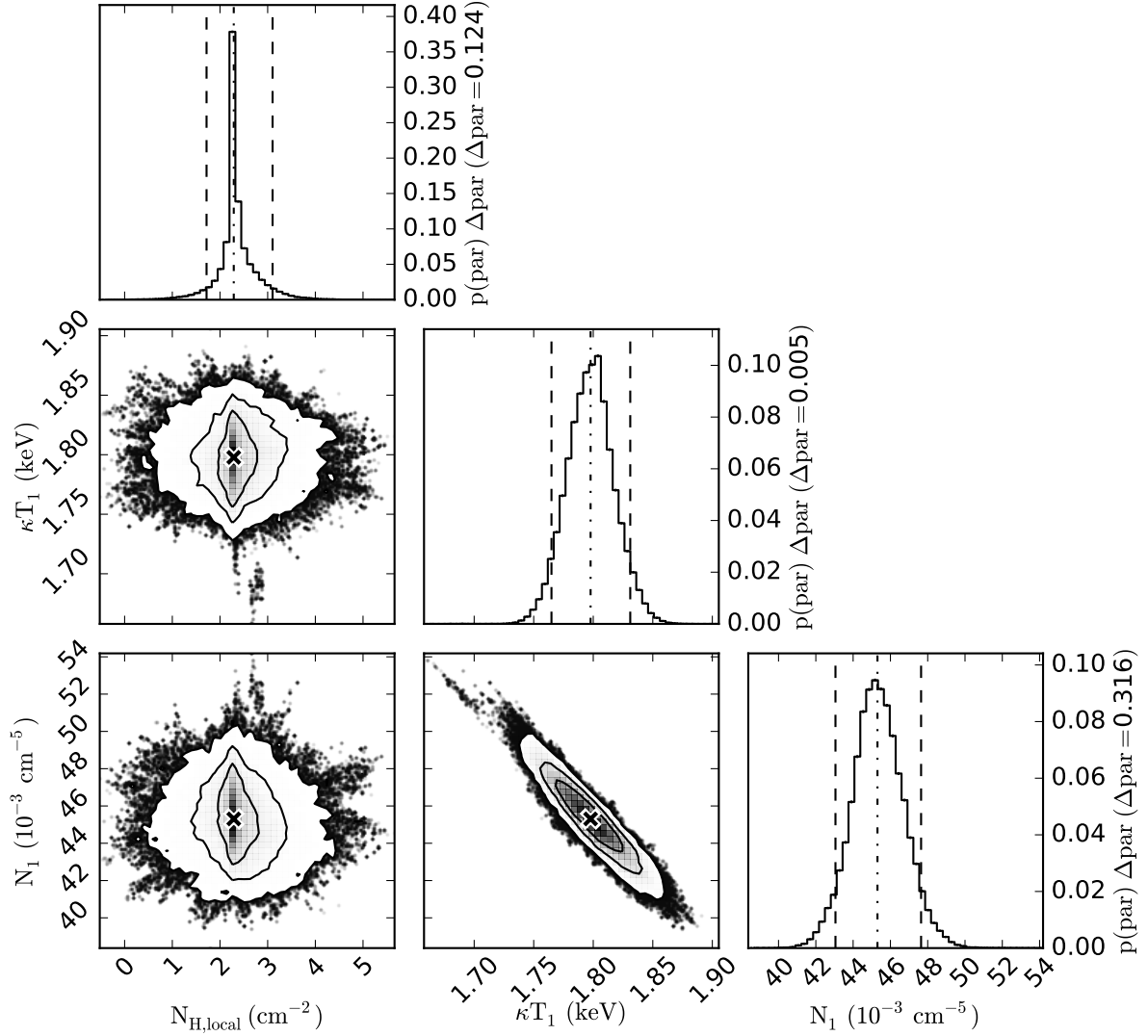


Figure A9. Triangle plot of the local hydrogen column density, the two temperatures and normalization parameters of the CND region. See caption of Fig. A1 for details. Note that the normalization parameters are not normalized by the extraction region area contrarily to those reported in Table 1.

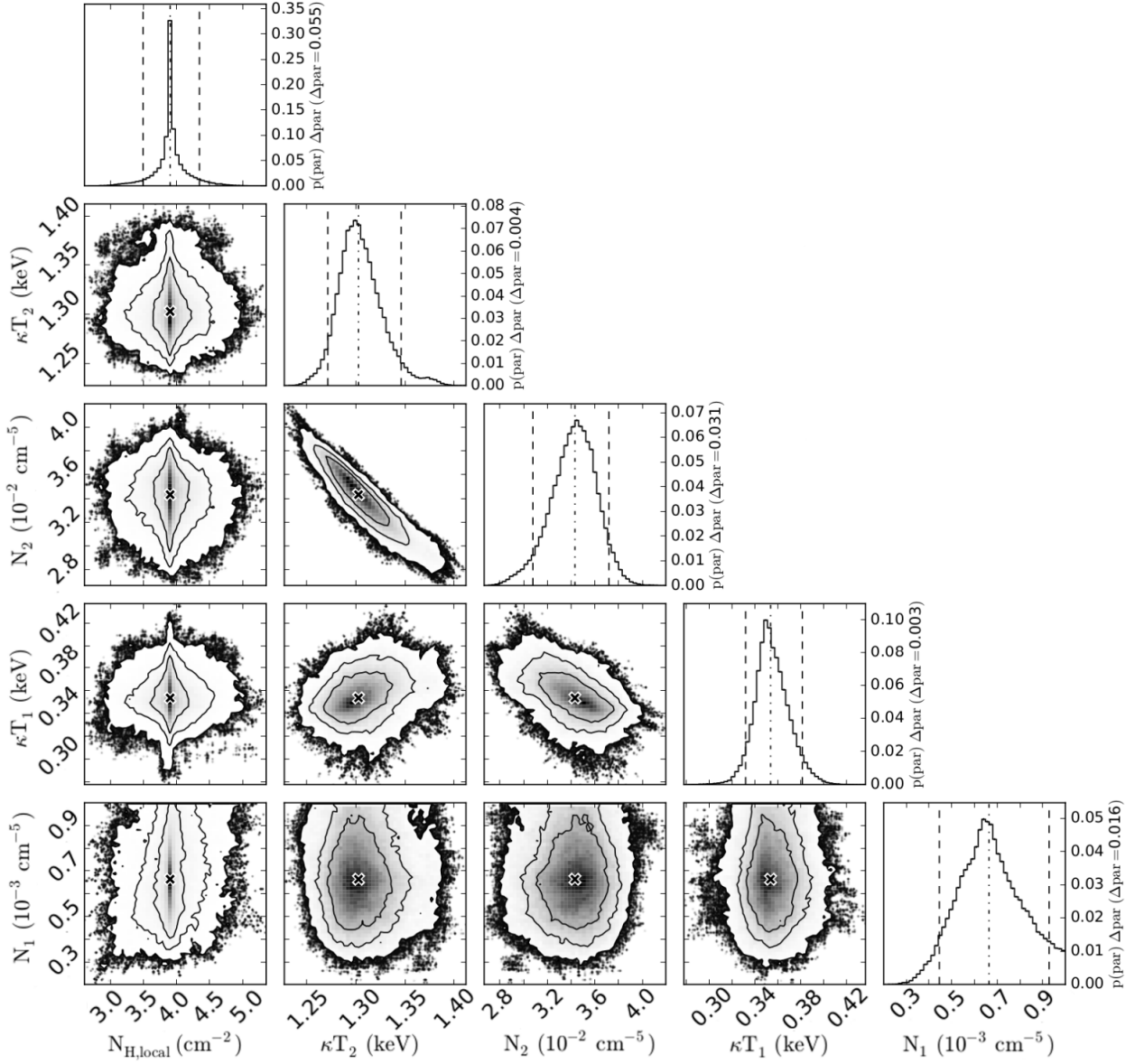


Figure A10. Triangle plot of the local hydrogen column density, the two temperatures and normalization parameters of the “outside” region. See caption of Fig. A1 for details. Note that the normalization parameters are not normalized by the extraction region area contrarily to those reported in Table 1.

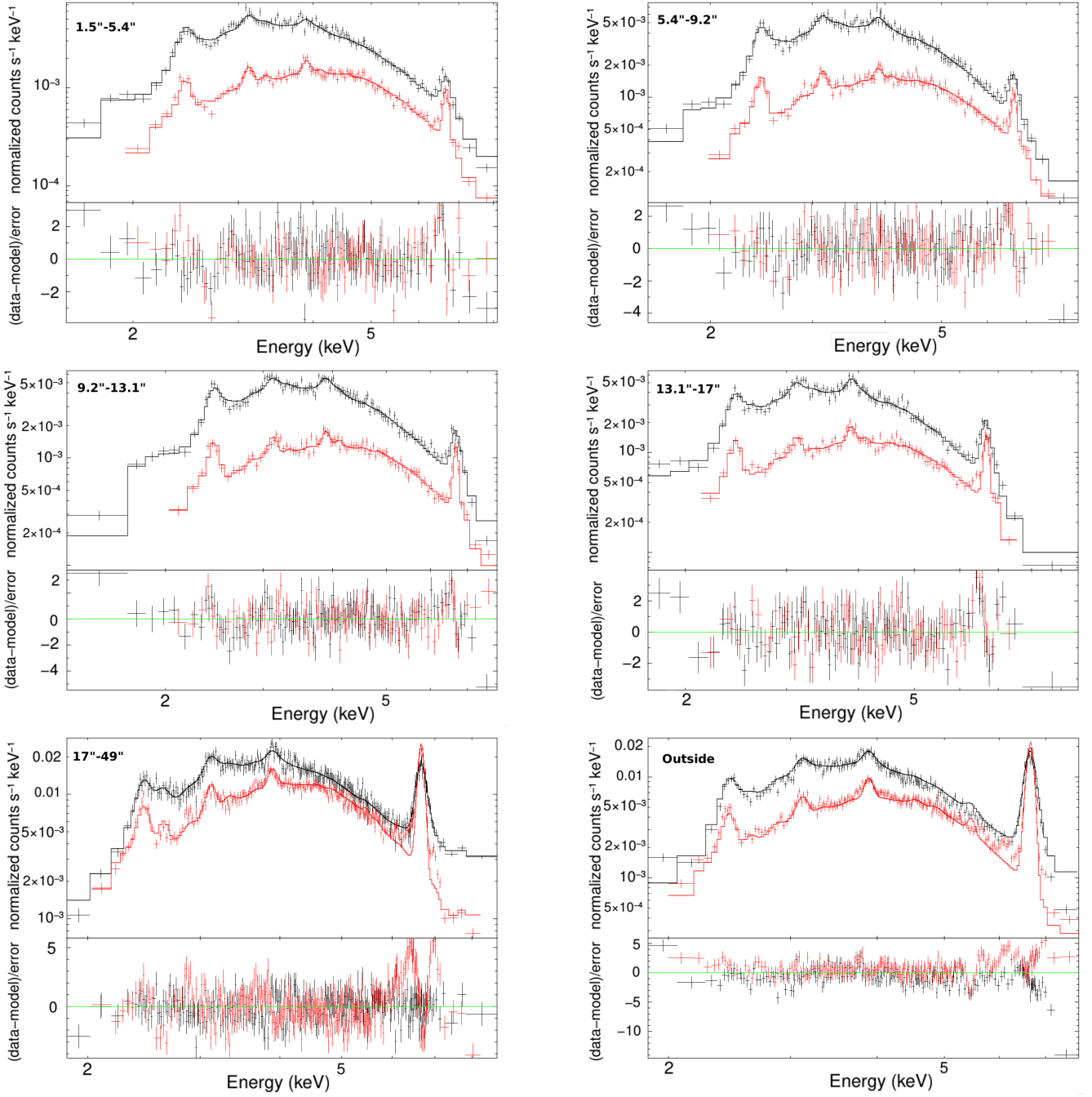


Figure A11. The best-fitting models for the X-ray diffuse emission spectra. The spectra were fitted with the `pileup*dustscat*TBnew*vphabs*(VAPEC+VAPEC)` model using the MCMC method with `XSPEC`. The crosses are the spectra observed with ACIS-I (black) and ACIS-S (red) grouped with a minimum signal-to-noise ratio of 5. The bottom panels are the deviation of the model from the data. (See online for colour version.)

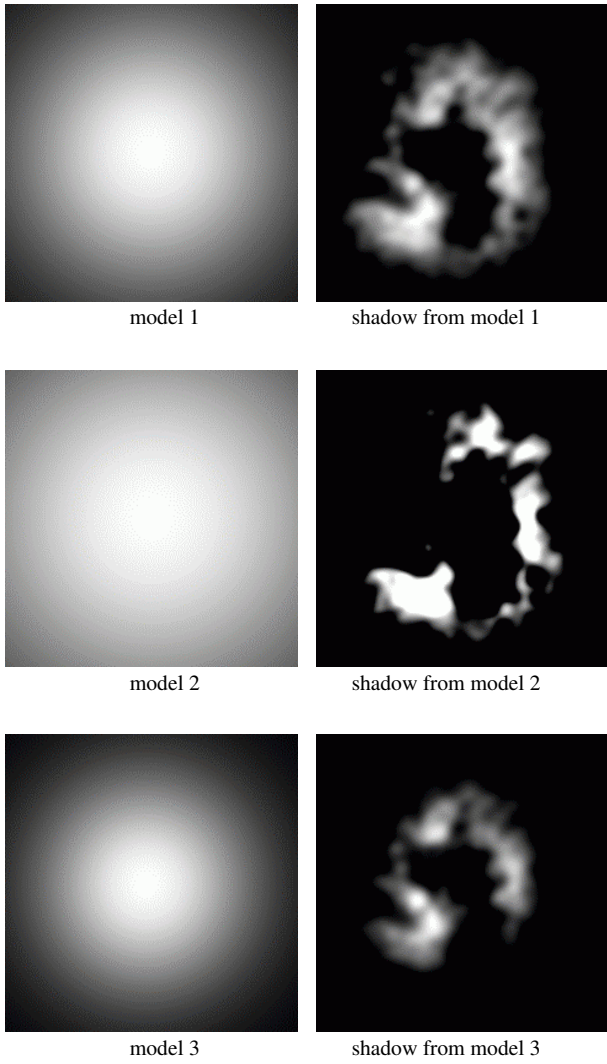


Figure B1. The three models for the X-ray diffuse emission and the derived shadow structure. Scales are the same as in Fig. 1 and Fig. 2.